

ADA 084014

Handwritten circled number 12

THE OPINIONS AND CONCLUSIONS CONTAINED IN THIS REPORT ARE THOSE OF THE AUTHORS AND SHOULD NOT BE INTERPRETED AS NECESSARILY REPRESENTING THE OFFICIAL POLICIES, EITHER EXPRESSED OR IMPLIED, OF THE ADVANCED RESEARCH PROJECTS AGENCY OR THE U.S. GOVERNMENT.

LEVEL II

ONE METER KrF LASER SYSTEM

J. C. Hsia, et al.
Avco Everett Research Laboratory, Inc.
2385 Revere Beach Parkway
Everett, MA 02149

Semi-Annual Technical Report for Period 25 May 1978 - 23 February 1979

APPROVED FOR PUBLIC RELEASE; DISTRIBUTION UNLIMITED.

Sponsored by
DEFENSE ADVANCED RESEARCH PROJECTS AGENCY
DARPA Order No. 3125

DTIC ELECTE
S MAY 9 1980 D
A

Monitored by
OFFICE OF NAVAL RESEARCH
DEPARTMENT OF THE NAVY
Arlington, VA 22217

FILE COPY

80 5 9 072

FOREWORD

DARPA Order No.: 3125

Contractor: Avco Everett Research Laboratory, Inc.

Effective Date of Contract: August 23, 1976

Contract Expiration Date: February 28, 1979

Contract No.: N00014-76-C-1032

Short Title of Work: One-Meter KrF Laser System

Principal Investigator and Phone No.: J.C. Hsia
(617) 389-3000, Ext. 551

Scientific Officer: Director Physics Program,
Physical Sciences Division
Office of Naval Research
800 North Quincy Street
Arlington, VA 22217

Amount of Contract: \$1,778,190

UNCLASSIFIED

SECURITY CLASSIFICATION OF THIS PAGE (When Data Entered)

REPORT DOCUMENTATION PAGE		READ INSTRUCTIONS BEFORE COMPLETING FORM
1. REPORT NUMBER	2. GOVT ACCESSION NO.	3. RECIPIENT'S CATALOG NUMBER
	AD-A084 024	
4. TITLE (and Subtitle)	5. TYPE OF REPORT & PERIOD COVERED	
ONE METER KrF LASER SYSTEM,	Semi-Annual Technical Rpt 25 May 1978 - 23 Feb. 1979	
	6. PERFORMING ORG. REPORT NUMBER	
	7. AUTHOR(s)	
J.C./Hsia, J.H./Jacob C./Duzy	8. CONTRACT OR GRANT NUMBER(s)	
	N00014-76-C-1032 DARPA Order - 3125	
9. PERFORMING ORGANIZATION NAME AND ADDRESS	10. PROGRAM ELEMENT, PROJECT, TASK AREA & WORK UNIT NUMBERS	
Avco Everett Research Laboratory, Inc. 2385 Revere Beach Parkway Everett, Massachusetts 02149	11. 23 Feb 79	
11. CONTROLLING OFFICE NAME AND ADDRESS	12. REPORT DATE	
Defense Advanced Research Projects Agency DARPA Order No. 3125		
	13. NUMBER OF PAGES	
	82	
14. MONITORING AGENCY NAME & ADDRESS (if different from Controlling Office)	15. SECURITY CLASS. (of this report)	
Office of Naval Research Department of the Navy Arlington, Virginia 22217	Unclassified	
	15a. DECLASSIFICATION/DOWNGRADING SCHEDULE	
16. DISTRIBUTION STATEMENT (of this Report)		
Approved for public release; distribution unlimited.		
17. DISTRIBUTION STATEMENT (of the abstract entered in Block 20, if different from Report)		
9 Semi-Annual Technical Rpt. 25 May 78 - 23 Feb 79		
18. SUPPLEMENTARY NOTES		
048450		
19. KEY WORDS (Continue on reverse side if necessary and identify by block number)		
Rare Gas-Halide Lasers Laser Modeling High Power UV Lasers Laser Kinetics KrF Lasers Mercury Halide Lasers XeF Lasers		
20. ABSTRACT (Continue on reverse side if necessary and identify by block number)		
This interim report covers research directed towards the development of efficient, high power, UV/visible lasers. The key issues being addressed are: (1) e-beam and e-beam controlled discharge excitation, (2) laser kinetics and modeling, (3) discharge stability and enhancement, (4) laser medium gain, adsorption and energy extraction, and (5) intrinsic laser efficiency and scaling. Using e-beam controlled discharge pumping of Hg/Cl ₂ /Ar mixtures, a HgCl		

DD FORM 1 JAN 73 1473

EDITION OF 1 NOV 65 IS OBSOLETE

UNCLASSIFIED

SECURITY CLASSIFICATION OF THIS PAGE (When Data Entered)

048450 24

UNCLASSIFIED

SECURITY CLASSIFICATION OF THIS PAGE(When Data Entered)

(20)

intrinsic laser efficiency of 3% was obtained at a specific energy of 1.4 J/liter. The laser performance was found to be adversely affected by high active medium absorption and poor branching into $HgCl^*$ from $3p_0$ and $3p_1$ states of Hg^* . The efficiency of e-beam excited KrF lasers was shown to improve with heating of the laser mixture. This improvement was shown to be consistent with the theoretically calculated reduction in three body quenching of KrF^* with increasing temperature. An XeF specific laser energy of 14 J/liter was achieved in 3 amagat mixture of $NF_3^1/Xe/Ne$ with 5% intrinsic efficiency. The rate constants for XeF ground state vibrational mixing and dissociation have been calculated theoretically. These calculations have been compared with experimental data.

Accession For	
NTIS	<input checked="" type="checkbox"/>
DDC PAS	<input type="checkbox"/>
UNCLASSIFIED	<input type="checkbox"/>
JEREMY	<input type="checkbox"/>
By	
Date	
Dist	
A	

UNCLASSIFIED

SECURITY CLASSIFICATION OF THIS PAGE(When Data Entered)

REPORT SUMMARY

A. PROGRAM SCOPE AND OBJECTIVES

This interim technical report describes DARPA/ONR-sponsored research, carried out during the period May 25, 1978 to February 23, 1979, directed towards the development of high power visible/UV lasers. The overall objectives of this research are to: (1) identify the key physical processes governing the operation of mercury and rare gas monohalide laser systems, and (2) experimentally verify laser performance and scaling predictions made by comprehensive laser models.

During this reporting period a portion of the effort was devoted to the study of e-beam controlled discharge pumping of HgCl lasers. Discharge pumping is attractive for this laser because of the possibility of a high Hg* production efficiency which may lead to a highly efficient, scalable laser in the visible.

Also in this period the effect of temperature on KrF laser operation was investigated using the one-meter laser device. High temperature KrF laser operation is expected to lead to improved laser efficiency because three-body quenching of KrF*, (the upper laser state), by Ar and Kr has been shown theoretically to decrease with increasing temperature.

In addition, experiments were performed to explore the limit of specific energy (J/liter) achievable in e-beam pumped XeF lasers. Specific energy has been shown to be critical in determining the cost of a large-scale device suitable for DARPA missions.

In parallel with the above, theoretical calculations were carried out for the rates of XeF ground state vibrational mixing and collisional dissociation as functions of temperature. The results of these calculations will be incorporated into a comprehensive XeF laser model code which will predict XeF laser performance and energy scaling.

B. ACCOMPLISHMENTS AND FINDINGS

The major accomplishments and findings obtained in this reporting period are summarized as follows:

- (1) E-beam controlled discharge experiments were carried out in Hg/Cl₂/Ar mixtures where no prereaction between Hg and Cl₂ was detectable.
- (2) An HgCl intrinsic laser efficiency of 3% was obtained with a discharge enhancement ratio of 11.
- (3) The measured small-signal gain and fluorescence efficiency under optimum laser conditions suggest poor HgCl* formation from Hg*(³P₀, ³P₁) reactions with Cl₂.
- (4) Active medium photoabsorption of Hg/Cl₂/Ar mixtures near the laser wavelength was measured using a probe laser and found to be large (0.4-0.8%/cm) under typical operating conditions.

- (5) The results of HgCl* laser experiments have been compared with model calculations and good agreement obtained.
- (6) KrF* and Kr₂F* fluorescence was measured versus temperature. The results are consistent with calculated temperature dependence of three body quenching of KrF* by Ar and Kr.
- (7) The KrF intrinsic laser efficiency was shown to improve with temperature.
- (8) Energy deposition per unit active laser volume was increased by using magnetic compression of the e-beam.
- (9) A XeF laser specific energy of 14 J/liter was achieved at 3 amagats (4.7 J/liter-amagats) with 5% intrinsic efficiency.
- (10) The XeF laser performance has been compared with model calculation.

TABLE OF CONTENTS

<u>Section</u>	<u>Page</u>
Report Summary	1
List of Illustrations	7
I. INTRODUCTION	9
II. E-BEAM CONTROLLED DISCHARGE PUMPED HgCl LASER EXPERIMENTS	12
A. Key HgCl Laser Issues	13
B. Hg/Cl ₂ Prereaction Studies	15
C. HgCl* Discharge Characteristics	20
D. HgCl Laser Experiments	34
E. Conclusions	40
III. IMPROVEMENT IN KrF LASER PERFORMANCE AT ELEVATED TEMPERATURES	43
IV. XeF LASER EXPERIMENTS	55
V. RATE CONSTANTS FOR GROUND STATE DEACTIVATION	65
A. Introduction	65
B. Theory	67
C. Rate Constant Results	71
D. Ground State Bottlenecking	74
REFERENCES	81

LIST OF ILLUSTRATIONS

<u>Figure</u>		<u>Page</u>
1	Cl ₂ and Hg Density Monitoring System	16
2	Hg(³ P) Production Efficiency vs Hg*/Hg Ratio at Various Electric Fields	22
3	Electron Impact Cross Sections for Ground and Excited States of Hg	23
4	HgCl Discharge Characteristics	27
5	Comparison of Calculated and Measured Discharge Voltage and Current Characteristics	33
6	Optimum Output Coupling vs αL and $g_0 L$	37
7	HgCl Laser Active Medium Absorption Measurement Apparatus	38
8	Experimental Arrangement Used to Measure KrF* and Kr ₂ F* Fluorescence vs Temperature	45
9	KrF* and Kr ₂ F* Fluorescence Intensity vs Temperature	46
10	KrF* Laser Efficiency vs Temperature	47
11	Calculated and Measured KrF* and Kr ₂ F* Fluorescence Intensities vs Temperature	50
12	Calculated and Measured Laser Output Energy vs Temperature	52
13	Projected KrF Laser Efficiency vs Temperature at Various Gas Densities	53
14	Cross Section of the Small Aluminum Heated Cell	58
15	Measured Intrinsic Laser Efficiency at Various Temperatures	60
16	Measured Intrinsic Laser Efficiency vs Initial and Final Temperatures	62

<u>Figure</u>		<u>Page</u>
17	E-Beam Calorimeter	63
18	Potential Energy Diagram for XeF Indicating the UV Lasing Transitions	66
19	Dissociative Rate Constants for XeF(x) State at 300°K	73
20	Dissociative Rate Constants for the XeF Ground State at 300°K and 450°K	75
21	Comparison between Experimental (x) and Theoretical (Hatched) Sidelight Fluorescence Results for 3 Amagats and an E-Beam Current Density of 8 A/cm ²	80

I. INTRODUCTION

The overall objective of the DARPA/ONR sponsored rare gas monohalide laser program is to determine whether this class of UV/visible lasers can be made both efficient and scalable to high average powers needed for achieving specific DARPA goals. In order to meet this objective various parts of the underlying physics governing these lasers are resolved, where possible, on small-scale devices. These experiments provide the various parameter values (cross sections, rate constants, etc.) which are used to develop comprehensive laser models. One-meter laser experiments are performed to first help identify the key processes that must be correctly modeled and, second, to experimentally verify that performance predictions made by model calculations can be achieved. Once the predictive capability of the models has been demonstrated then these laser models can be used to accurately assess the performance achievable with larger scale versions of these lasers.

In the previous reporting period one-meter experiments were performed to explore the performance of XeF lasers at elevated temperatures. These experiments have led to the demonstration of intrinsic XeF laser efficiencies of $> 5\%$. Experiments were also carried out to study energy extraction, gain saturation and triatomic formation in KrF lasers. The results of these

experiments have been compared in detail to predictions of a comprehensive KrF laser model. The comparisons have shown that for pulselengths > 250 ns and e-beam excitation intensities < 0.5 MW/cm³, the model correctly predicted laser performance over a wide range of operating conditions.

In this reporting period the one-meter device has been used to study e-beam controlled discharge pumping of the HgCl laser. This laser, with output at 5576 \AA , was discovered at AERL under direct e-beam excitation.⁽¹⁾ With e-beam pumping its efficiency was low, principally due to the low quantum efficiency and poor energy channeling from e-beam ionization into HgCl*, the lasing species.

It was recognized from the outset that with discharge pumping the ultimate efficiency can be much higher if Hg*, which can be efficiently made in a discharge, can be used to form HgCl* via a "harpooning" reaction with a suitable chlorine donor. More recently HgCl* has been made to lase in a discharge^(2,3) using Cl₂ as the donor in small-scale experiments. These experiments have been seriously hampered by wall catalysed pre-reaction problems between Hg and Cl₂. However, the rate for this reaction is sufficiently slow,⁽⁴⁾ especially on teflon-coated surfaces, that in a large scale device such as the one-meter

(1) Parks, J.H., Appl. Phys. Lett. 31, 192 (1977).

(2) Tang, K.Y., et al., Appl. Phys. Lett. 32, 226 (1978).

(3) Mangano, J.A., Jacob, J.H., Private Communication.

(4) Medhekar, A.K., et al., Chem. Phys. Lett. 65, 600 (1979).

device, with a favorable volume to surface ratio, sufficient time should be available to perform the experiment before appreciable prereaction occurred if care is taken.

The purpose of these experiments was to study the dominant processes (e.g., discharge stability, HgCl^* formation, excited species absorption, etc.) governing the operation of this laser and to demonstrate efficient energy extraction. These experiments and results obtained are discussed in Section II.

Also in this reporting period the one-meter device was used to study the performance of e-beam pumped KrF lasers at elevated temperatures. The efficiency of KrF lasers was expected to improve at elevated temperatures because the rate of three-body quenching of KrF^* by Kr and Ar should decrease with increasing temperature.⁽⁵⁾ Reduced KrF^* quenching would lead to increased small-signal gain, increased KrF^* fluorescence efficiency and decreased formation of the triatomic Kr_2F^* which is an absorber at the laser wavelength. The objectives of the one-meter experiments were to verify reduced KrF^* quenching, reduced Kr_2F^* formation at elevated temperatures, and demonstrate improved laser efficiency. The results of these experiments are discussed in Section III.

In Section IV we report on further XeF laser experiments performed to explore critical specific energy (J/liter) issues. It had been shown that besides efficiency the most critical

(5) Shui, V.H., Appl. Phys. Lett. 34, 203 (1979).

parameter in determining the cost of a large-scale repetitively pulsed XeF laser is specific energy.⁽⁶⁾ Previous experiments had been directed towards achieving high intrinsic laser efficiency. The issue of specific pulse energy had not been adequately addressed, primarily due to limitation of specific energy deposition when cold cathodes are used. In the experiments described here magnetic compression of the e-beam was used to increase the specific energy deposition in the laser mixture.

In parallel with the above, theoretical calculations continued on the rate constants for XeF ground state deactivation. The effects of vibrational/rotational energy and temperature on these rate constants have been included in these calculations. The results of these calculations will be used in the XeF laser model code. These calculations are summarized in Section V.

(6) Jacob, J.H., Private Communication.

II. E-BEAM CONTROLLED DISCHARGE PUMPED HgCl LASER EXPERIMENTS

A. KEY HgCl LASER ISSUES

HgCl* was first made to lase on the $B^2\Sigma^+_{1/2} \rightarrow X^2\Sigma^+_{1/2}$ transition at AERL under DARPA/ONR sponsorship.⁽¹⁾ The $B^2\Sigma^+_{1/2}$ upper state is predominantly ionic in character, correlating with separated ions $Hg^+(^2S_{1/2}) + Cl^-(^1S_0)$. This ionic character provides the opportunity for efficient formation similar to that found in the rare-gas monohalide lasers. The $X^2\Sigma^+_{1/2}$ state is covalent in nature and bound by 1.04 eV. Although the lower state is bound, the lasing transition terminates in high vibrational levels ($v'' = 21, 22$) of HgCl, thus rapid lower state removal may be possible through vibrational relaxation into lower vibrational levels. These characteristics make HgCl* an attractive candidate for a highly efficient laser in the visible.

The first HgCl laser experiments were carried out using direct e-beam excitation. The efficiency achieved was low predominantly due to the low HgCl* production efficiency by the e-beam. However, it was recognized from the outset that if discharge pumping can be used, much higher efficiencies should be possible.⁽¹⁾

In a discharge, Hg*(6p) states can be pumped efficiently. Conditions can be chosen so that > 90% of the discharge energy

is deposited to make $\text{Hg}^*(6p)$ states. Hg^* can then be used to make HgCl^* via harpooning reactions with a suitable chlorine donor. If this can be achieved with near unity branching, then the maximum HgCl^* formation efficiency can be as high as 40%. In comparison, the corresponding maximum formation efficiency is 8.6% with direct e-beam excitation.

Of the possible chlorine donors Cl_2 is attractive because, first, it does not absorb at 5576 \AA , and second, the low binding energy of Cl_2 allows HgCl^* to be accessed energetically from all the spin orbit states of $\text{Hg}^*(6p)$. Also its attachment rate is appropriate and deactivation of Hg^* is rapid.

To date e-beam controlled discharge experiments using Cl_2 had been hampered by Hg and Cl_2 spontaneous reaction problems. Experiments had shown that this reaction does not occur directly in the vapor phase but rather on material surfaces⁽⁴⁾ and therefore is not a fundamental limitation in the system. However, in a static fill experiment care must be taken to insure that the initial laser mixture contains Hg and Cl_2 rather than some reaction product. In the one meter heated cell described previously⁽⁷⁾ with its relatively large volume-to-surface area ratio and teflon-coated walls, it should be possible to carry out discharge experiments before significant prereaction occurs. This is demonstrated by a series of prereaction studies described below.

(7) Mangano, J.A., et al., "One-Meter KrF Laser System" Semi-Annual Report, November 24, 1977 to May 24, 1978.

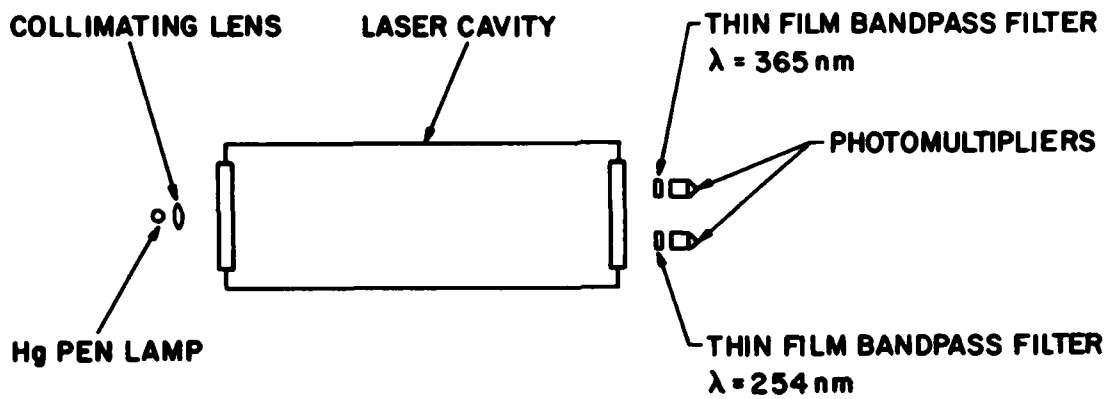
The purpose of the one-meter HgCl laser experiment was to study the key efficiency issues important in discharge-pumped HgCl lasers using Cl₂ as the chlorine donor. These included (1) discharge stability, (2) discharge enhancement, (3) Hg*(6p) formation efficiency, (4) HgCl* formation efficiency, and (5) laser energy extraction (absorption, upper and lower level kinetics).

B. Hg/Cl₂ PREREACTION STUDIES

In a previous small-scale experiment⁽⁴⁾ designed to study spontaneous reaction between Hg vapor and Cl₂, it was shown that (1) Hg and Cl₂ did not react spontaneously in the vapor phase, (2) the reaction took place on material surfaces, (3) the rate of the reaction depended on diffusion rate and surface material, (4) the reaction was particularly slow on nickel and teflon surfaces, and (5) typical reaction time is of order 60 sec for a 2.5 cm cell at 1 atm.

Scaling from the above experiments, assuming that surface reactions are controlled by diffusion of Hg to the cell walls, the estimated time for appreciable reaction in the one meter device is > 30 min. However, the validity of this estimate depends on the turbulence generated in filling the cell and subsequent convection arising from temperature nonuniformities in the cell.

The experimental arrangement used to measure the time available before appreciable prereaction occurred upon mixing the Hg and Cl₂ is shown in Figure 1. A Hg pen lamp was used as a source of 365 nm and 254 nm radiation. The transmission of these through



J4026

Figure 1. Cl_2 and Hg Density Monitoring System

the laser cell was measured by two narrow band filtered photomultipliers. The 365 nm transmission was used to monitor the Cl_2 concentration. The 254 nm line was used as a qualitative indication of Hg concentration. For typical Hg concentrations the laser cell was black to the bulk of the 254 nm line. Only radiation far out in the wings of the 254 nm Hg lamp line profile transmitted through the cell. To relate this transmission to cell Hg concentration was difficult. It is for this reason that the 254 nm transmission was used only as an indication of gross changes in Hg density. The cell was first passivated using a 1% F_2 /99% Ar mixture. Then the reactivity of the cell to Cl_2 /Ar mixture without Hg was measured. When the cell walls were clean (uncontaminated by Hg reaction products) no change in Cl_2 concentration was detected with 365 nm absorption for up to 20 min. Furthermore, the Cl_2 concentration deduced using the measured absorption through the cell and published Cl_2 absorption cross section, agreed with the Cl_2 concentration in the initial mixture to within 5%.

For prereaction studies the cell was filled first with Hg to the desired pressure by opening the valve to the Hg reservoir. The Hg partial pressure was determined by the reservoir temperature. The temperature of the cell was maintained at least 20°C above the reservoir temperature to avoid recondensation. The Cl_2 was introduced into the cell, premixed with Ar and preheated to the cell temperature, through a teflon coated piccolo. Typical filling times for 2 amagat total cell gas density was 10 s.

The cell was found to operate in three distinct modes. Initially, with the cell walls uncontaminated by reaction products, mixtures of up to 50 Torr Hg, 15 Torr Cl₂ and balance Ar at a total density of 2.5 amagats introduced into the cell exhibited no detectable changes in Hg or Cl₂ densities for up to 10 min. The 254 nm transmission of the cell showed no Hg density change upon the introduction of the Cl₂/Ar mixture. Furthermore, the magnitude of the 365 nm absorption agreed with that calculated from the known Cl₂ absorption cross section.

After ~ 20 fill/pump out cycles with Hg/Cl₂/Ar mixtures, the cell rapidly degraded into a mode where the 365 nm Cl₂ absorption indicated total Cl₂ disappearance within 5 s after completion of fill sequence. Simultaneously, the 254 nm cell transmission indicated some Hg depletion. Visual inspection of the cell walls at this time revealed the appearance of fine gray powder coating the walls throughout the cell.

Further operation of the cell resulted in a third mode where upon filling the cell with Cl₂/Ar mixture the cell became totally opaque to both 254 nm and 365 nm radiation. Visually a brown fog was observed in the cavity.

A complete scrubbing the cell walls and the gas feedlines was found to be sufficient to restore the cell to the condition where again no significant reaction was observable within the active laser volume for 10 min. The Hg pen lamp and photodetector Cl₂/Hg monitoring system was then installed to continuously monitor the condition of the cell throughout the laser experiments. The

cell was periodically dismantled and cleaned when necessary to ensure that laser experiments were carried out under conditions where the prereaction was negligible.

The observation described above is consistent with the previous conclusion that Hg and Cl₂ do not react spontaneously in the gas phase. The prereaction problems encountered when the cell walls were contaminated by reaction products can be attributed to fine particles generated on the walls which are sites where surface reaction can rapidly occur. No attempt was made to understand this mechanism in detail. Rather, we simply maintained cell cleanliness so that prereaction was not a problem. In a repetitively pulsed laser where flow would be required, this problem may be avoided by a suitably designed gas flow/mixing system.

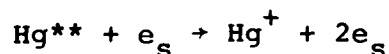
C. HgCl* DISCHARGE CHARACTERISTICS

E-Beam controlled discharge experiments were carried out in Ar/Hg/Cl₂ mixtures to study discharge stability, discharge enhancement and HgCl* production efficiency. The characteristics of such discharges had been analyzed theoretically.⁽⁸⁾ Before presenting the experimental results we briefly review some of the key conclusions of the theoretical analysis.

In a discharge Hg*(6P) states are produced via



where e_s are the secondary discharge electrons which are heated by the applied electric field. It had been shown that, in the regime of interest for HgCl lasers, the efficiency of producing Hg* states depends critically on the ratios of Hg* density to Hg density and Hg** density to Hg* density. As these ratios increase more energy is channeled into

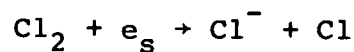


where Hg** denote higher excited (7^3S , 7^3P , 6^3D) states of Hg. The Hg* production efficiency can be calculated via a Boltzmann calculation as a function of Hg*/Hg density ratio with Hg**/Hg* as a parameter. An example of such a calculation is shown in

(8) Srivastava, B.N., et al., Appl. Phys. Lett. 32, 705 (1978).

Figure 2. For this calculation we have used the electron impact cross-sections calculated by Hyman.⁽⁹⁾ These are shown in Figure 3.

It has also been shown that for regimes of interest the discharge stability is governed by the rate of discharge ionization of Hg**. In order for a quasi-steady-state discharge to exist this ionization must be balanced by dissociative attachment,



The steady-state electron density in this case is then given by

$$n_e = \frac{S_{eb}}{\beta n_{\text{Cl}_2} - \nu_{i0}} \quad (1)$$

where S_{eb} is the e-beam ionization rate, β is the dissociative attachment rate constant for Cl_2 , n_{Cl_2} is the Cl_2 density and ν_{i0} is the equilibrium ionization rate by the discharge electrons. For discharge stability it had been shown that necessary conditions are

$$\beta n_{\text{Cl}_2} \geq 3\nu_{i0} \quad (2)$$

and

$$S_{eb} > 0 \quad (3)$$

(9) Hyman, H.A., Private Communication.

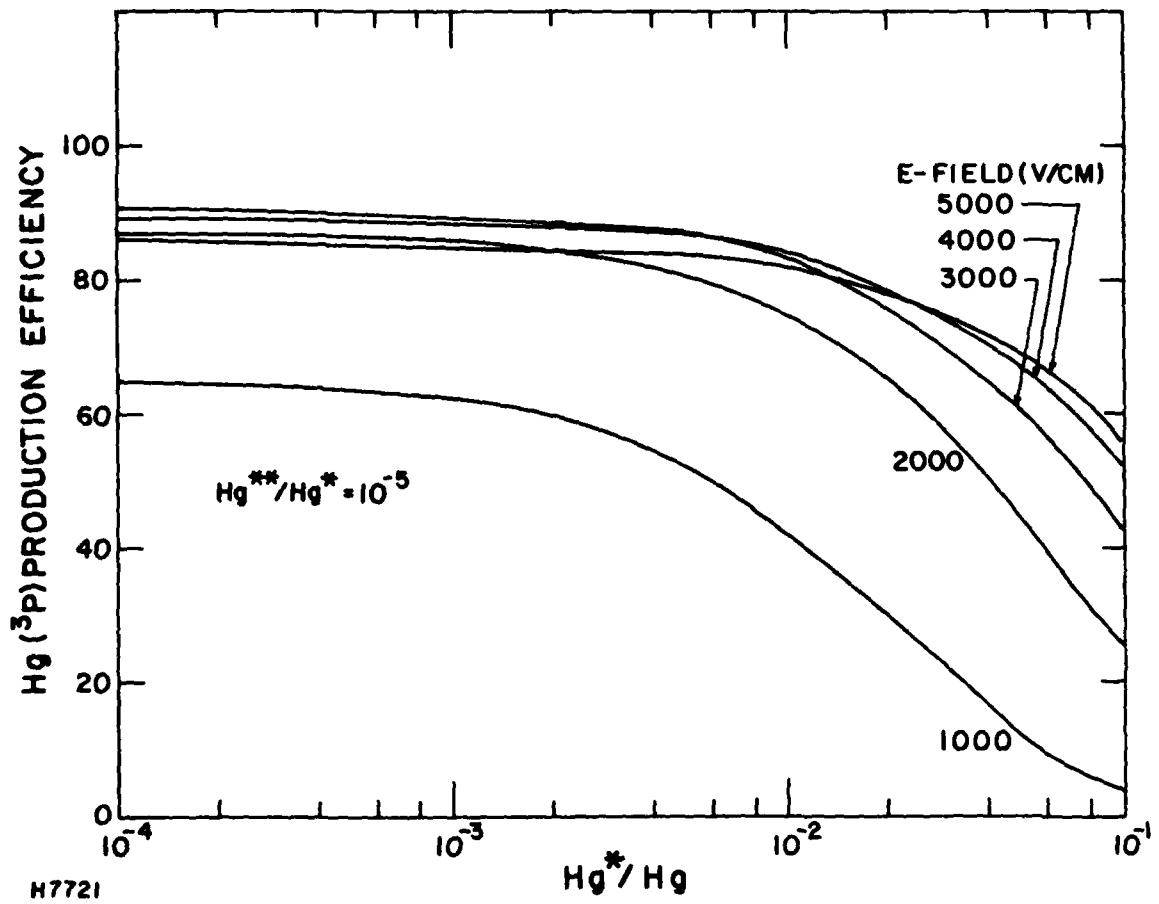
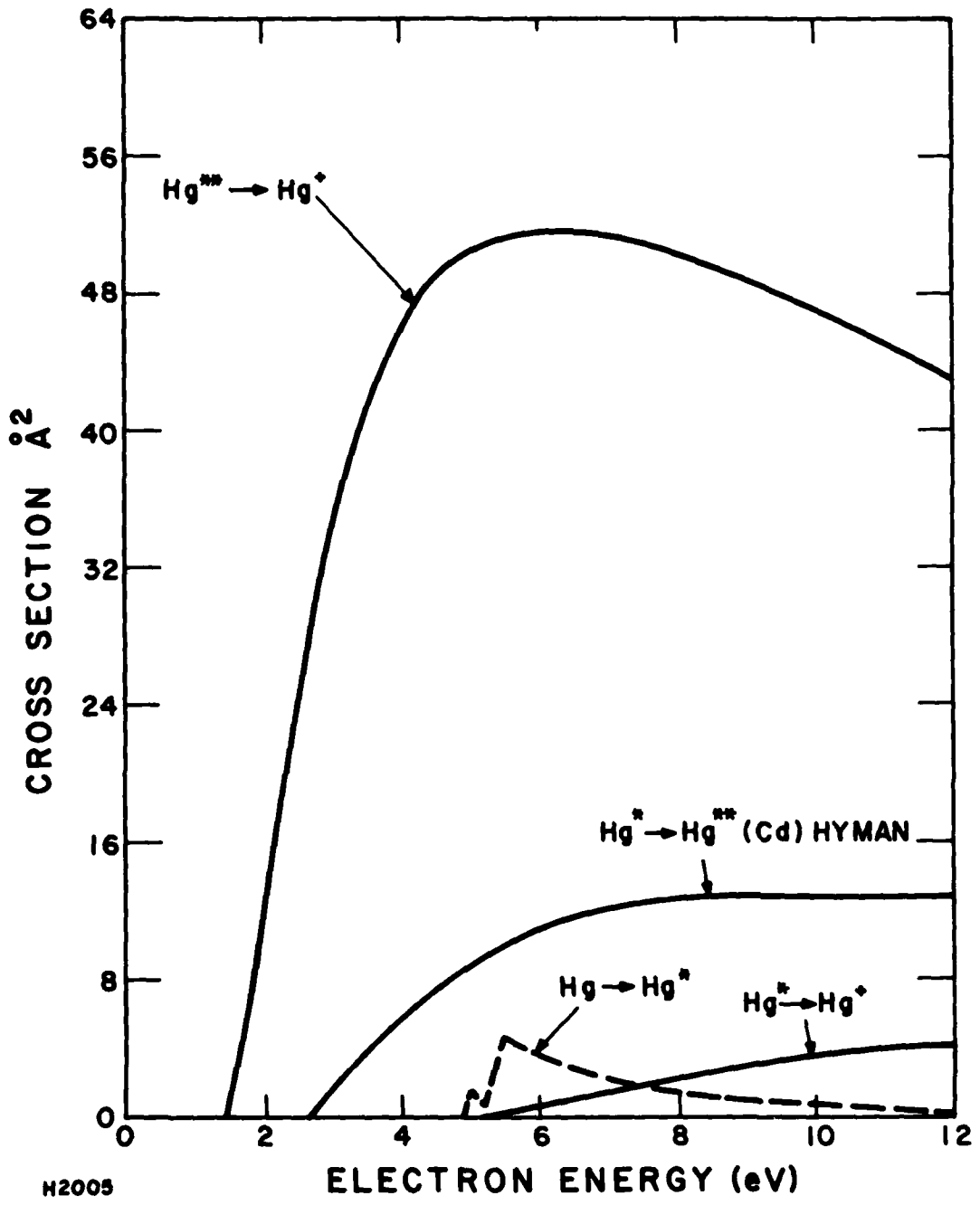


Figure 2. Hg(³P) Production Efficiency vs Hg*/Hg Ratio at Various Electric Fields



H2005

Figure 3. Electron Impact Cross Sections for Ground and Excited States of Hg

The discharge enhancement ratio, R_d , defined as the ratio of discharge power deposited to the e-beam power deposited in the mixture is given by

$$R_d = \frac{J E}{S_{eb} E_i} = \frac{e n_e V_d E}{S_{eb} E_i} \quad (4)$$

where V_d is the electron drift velocity in the applied field E , and E_i is the average e-beam energy required to make an electron-ion pair. Equations (1), (2) and (4) give

$$R_d \leq \frac{3}{2} \frac{e V_d E}{\beta n_{Cl_2} E_i} \quad (5)$$

Therefore, for discharge stability, the maximum R_d achievable varies inversely with the attachment rate βn_{Cl_2} . However, the Cl_2 density must be kept high in order to keep Hg^* and Hg^{**} densities low for a given discharge power density since v_{i0} is proportional to Hg^{**} density and Eq. (2) must be satisfied.

Furthermore, since Hg density must be kept low to minimize Hg quenching of $HgCl^*$, the lasing species, the requirement of low Hg^*/Hg and Hg^{**}/Hg^* ratios for efficient Hg^* production puts a lower bound constraint on the Cl_2 density required. All the above lead to tradeoffs in R_d , the input power density and Hg^* production efficiency. High discharge power density can only be maintained at low discharge enhancements. This is analogous to rare gas halide discharges studied previously. (10)

(10) Hsia, J.C., et al., "One-Meter KrF Laser System," Semi-Annual Report, Feb. 23, 1977 to Aug. 22, 1977.

To accurately model the discharge characteristics one needs: (1) the electron attachment rate constant for Cl_2 , (2) the quenching rate constant for Cl_2 on Hg^* and Hg^{**} , and (3) the electron impact cross section of Cl_2 . β for Cl_2 has been measured in a previous experiment.⁽¹¹⁾ The Hg^* quenching rate constant for Cl_2 has been measured for only one, ($^3\text{P}_2$) spin orbit state of Hg^* . The quenching rate constant for ($^3\text{P}_1$) and ($^3\text{P}_0$) states have not been measured. The quenching rate constants for the higher excited state are also not known. The low energy (0 to 10 eV) electron impact cross section of Cl_2 has not been measured.

For our model calculations we have assumed that the quenching rates for Cl_2 on all the $\text{Hg}^*(^3\text{P})$ states and Hg^{**} states are the same with a value of $4 \times 10^{-10} \text{ cm}^3/\text{s}$ which corresponds to that measured for ($^3\text{P}_2$).⁽¹²⁾ We have also approximated the Cl_2 electron impact cross section by using that of O_2 . With these approximations the calculations showed that for discharge power density of order 10^5 W/cm^3 , a R_d of ~ 10 can be stably achieved with Hg^* production efficiency $\approx 90\%$. The required Cl_2 density is calculated to be of order 2×10^{17} . A discharge power density of 10^5 W/cm^3 is required in order to achieve a specific laser energy of 10 J/liter assuming an intrinsic laser efficiency of 10% and a pulselength of 1 μs . In this case the

(11) Rokni, M., Jacob, J.H., Mangano, J.A., Appl. Phys. Lett. 34, 197 (1979).

(12) Krause, H.F., et al., Chem. Phys. Lett. 31, 577 (1975).

required e-beam power density is 10^4 W/cm³ which in 2 amagat of Ar corresponds to an e-beam current density of ~ 0.5 A/cm² at 250 kV.

Discharge experiments were carried out to study this regime. Typical discharge V-I characteristics obtained are shown in Figure 4. Figure 4(a) are oscillograms of the e-gun cathode voltage and transmitted cell current density. The peak e-beam voltage was 250 kV and the pulselength was 900 ns. The e-beam current continually increased during the pulse due to diode closure and the peak cell current density was 1.1 A/cm². The discharge anode-cathode spacing was 5 cm and the discharge cross section was 100 cm x 9 cm. Figures 4(b), (c) and (d) are discharge voltage and current oscillograms taken at various applied voltages. For all the pulses shown, the discharge voltage was applied 200 ns after the start of the e-beam pulse. The discharge circuitry has been described previously.⁽¹⁰⁾

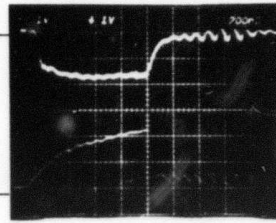
Figure 4(b) shows a typical stable discharge where the discharge voltage was maintained at a relatively constant value throughout the pulse. The discharge current increased during the pulse due to the increase in e-beam current and destruction of Cl₂ during the pulse. When the e-beam was turned off the discharge current first began to turn off, but the inductance in the external circuitry induced a voltage spike across the discharge and the discharge went unstable. The discharge went into an arc and the discharge voltage then collapsed and the current was limited only by the external circuitry.

0.4% Cl₂/1% Hg/98.6% Ar AT 2 AMAGATS

(A)
E-BEAM
CHARACTERISTICS

VOLTAGE
150 kV/div

CURRENT
DENSITY
500 A/div

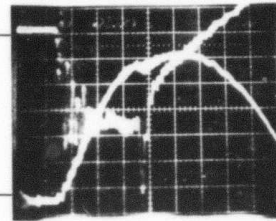


DISCHARGE
CHARACTERISTICS

(B)

VOLTAGE
4.4 kV/div

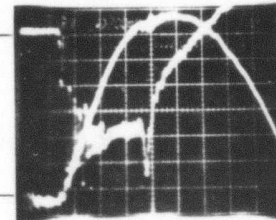
CURRENT
14 kA/div



(C)

VOLTAGE
4.4 kV/div

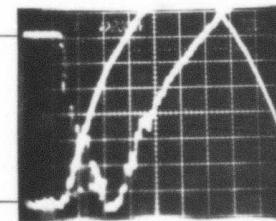
CURRENT
14 kA/div



(D)

VOLTAGE
4.4 kV/div

CURRENT
14 kA/div



J4024

→ 200 nS/div

Figure 4. HgCl Discharge Characteristics

Figure 4(c) shows a shot close to the limit of discharge stability, where near the end of the pulse the discharge voltage began to decrease. For this shot the peak discharge current density was 92 A/cm^2 at a discharge electric field of 3.3 kV/cm which corresponded to a discharge enhancement ratio of 12.

Figure 4(d) shows a shot where volumetric instability occurred during the pulse. When that happened, the discharge voltage quickly collapsed and the current became limited only by the external circuitry.

The HgCl^* fluorescence was measured with a calibrated photodiode through a bandpass filter of known transmission. For conditions of Figure 4(c), the fluorescence intensity at the peak of the discharge current pulse was 9.5 kW/cm^3 which corresponded to a HgCl^* fluorescence efficiency of 3.1%.

The HgCl^* production efficiency in the discharge can be estimated from the measured HgCl^* fluorescence efficiency using the equation

$$\eta_{\text{form}} = \eta_{\text{fl}} (1 + \tau_s k_{\text{Cl}_2} n_{\text{Cl}_2} + \tau_s k_{\text{Hg}} n_{\text{Hg}} + \tau_s k_{\text{Ar}} n_{\text{Ar}} + \tau_s k_e n_e) \quad (6)$$

where η_{form} is the efficiency of producing HgCl^* by the discharge, η_{fl} is the fluorescence efficiency, τ_s is the spontaneous lifetime of HgCl^* , the k 's are the various heavy particle and electron quenching rate constants, and the n 's are the densities. $\tau_s k_{\text{Ar}}$

and $\tau_s k_{Cl_2}$ have been measured by Mandl and Parks⁽¹³⁾ and $\tau_s k_{Hg}$ has been measured by Parks and Klimek.⁽¹⁴⁾ The measured values are listed in Table 1. The electron quenching rate constant, k_e , has not been measured.

In Table 2 the various terms in Eq. (6) are calculated for the experimental conditions of Figure 4(c). For the electron quenching term we have estimated the rate by using the rate constant measured for KrF^* of $2 \times 10^{-7} \text{ cm}^3/\text{s}$. The electron density n_e was estimated to be 2.1×10^{14} in this case. Equation (6) then suggests a $HgCl^*$ formation efficiency of $\approx 13\%$.

If for every $Hg^*(^3P)$ state produced by the discharge, a $HgCl^*$ was made, then a $HgCl^*$ formation efficiency of 13% implies a Hg^* production of $\approx 29\%$. (The quantum efficiency of producing $HgCl^*$ which has 2.23 eV of energy, from Hg^* which has 5 eV energy, is 45%.) For the conditions of the experiment the model calculations predicted of a $Hg^*(^3P)$ production efficiency of 90% which is over three times that deduced from $HgCl^*$ formation assuming unit branching from Hg^* into $HgCl^*$.

The reaction of $Hg^*(^3P_2)$ with Cl_2 has been measured and shown to lead to $HgCl^*$ formation with near unit branching.⁽¹²⁾ The reaction of $Hg^*(^3P_0, ^3P_1)$ states with Cl_2 to form $HgCl^*$ is exothermic and are energetically allowed. $HgCl^*$ fluorescence has been seen from $Hg^*(^3P_0)$ reacting with Cl_2 .⁽¹⁵⁾ However,

(13) Mandl, A. and Parks, J.H., Appl. Phys. Lett. 33, 498 (1978).

(14) Parks, J.H. and Klimek, D., Unpublished.

(15) Mandl, A., Private Communication.

TABLE 1. HgCl* QUENCHING RATE CONSTANTS

Q	$k_Q \tau_s$	$k_Q (\tau_s = 29 \text{ ns})$
Ar	$< 3 \times 10^{-22}$	
Cl ₂	3.8×10^{-18}	1.3×10^{-10}
Hg	1.2×10^{-18}	4×10^{-11}

TABLE 2. CONTRIBUTIONS TO HgCl* QUENCHING

$k_{\text{Ar}} \tau_s n_{\text{Ar}}$	< 0.02
$k_{\text{Cl}_2} \tau_s n_{\text{Cl}_2}$	0.874
$k_{\text{Hg}} \tau_s n_{\text{Hg}}$	1.13
$k_e \tau_s n_e$	1.22 ($k_e = 2 \times 10^{-7} \text{ cm}^3/\text{s}$)

the branching ratios for HgCl* production are not known for either 3P_1 or 3P_0 states. A likely explanation for the observed low HgCl* production in our discharge experiment is that the branching from both of these states into HgCl* were low (< 0.1). Such low HgCl* formation can be due possibly to a potential barrier in the 3P_0 and 3P_1 reaction channels but not in the 3P_2 channel.

For discharge conditions of Figure 4(c), the Boltzmann code calculated a Hg*(3P_2) formation efficiency of $\approx 50\%$. Of those Hg*(3P_2) states made, kinetic model calculations showed that only $\approx 60\%$ of them react to form HgCl* because the competing electron impact rate



was roughly equal to the Cl₂ quenching rate of Hg*(3P_2). The predicted HgCl* formation efficiency is then 14%, which is consistent with that deduced from the HgCl* fluorescence.

Circuit equations which describe the external discharge circuitry used in these experiments have been incorporated into our HgCl* discharge model code. The code can thus predict the self-consistent electric field and current density in the discharge for a given initial gas mixture, charge voltage on the discharge supply capacitor bank, and e-beam current density. A comparison between the measured discharge voltage, and current characteristics and those predicted by the model, up to the time

of e-beam pulse termination, is shown in Figure 5. The agreement is within 20%. After the e-beam was switched off the discharge went into an arc, and the code was no longer valid in that regime.

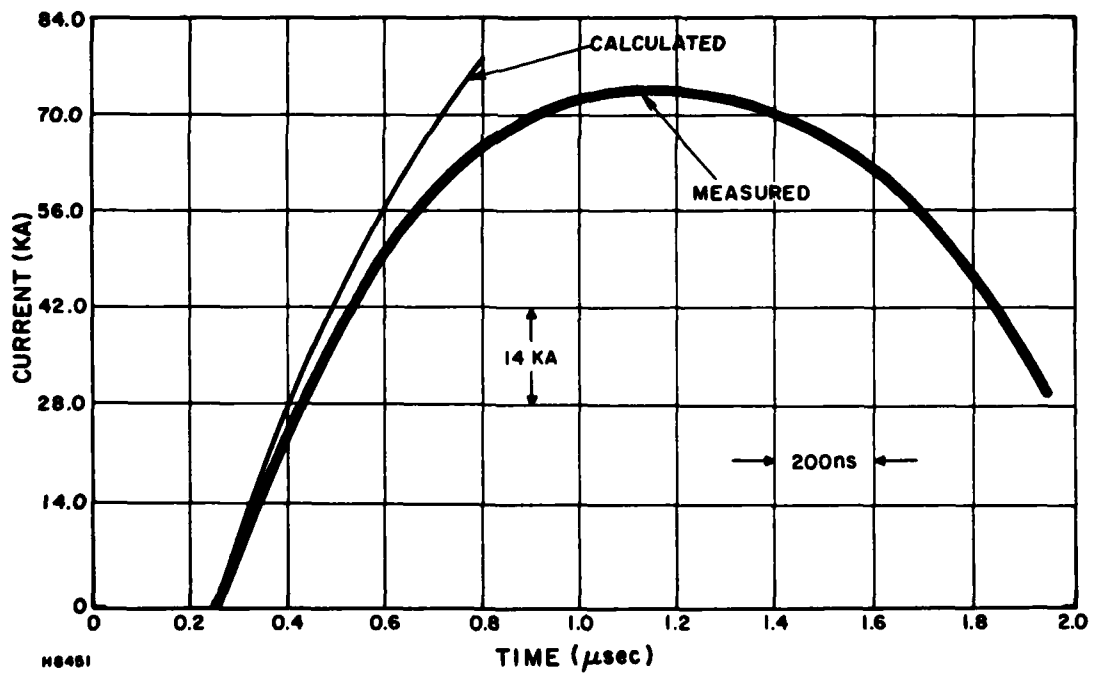
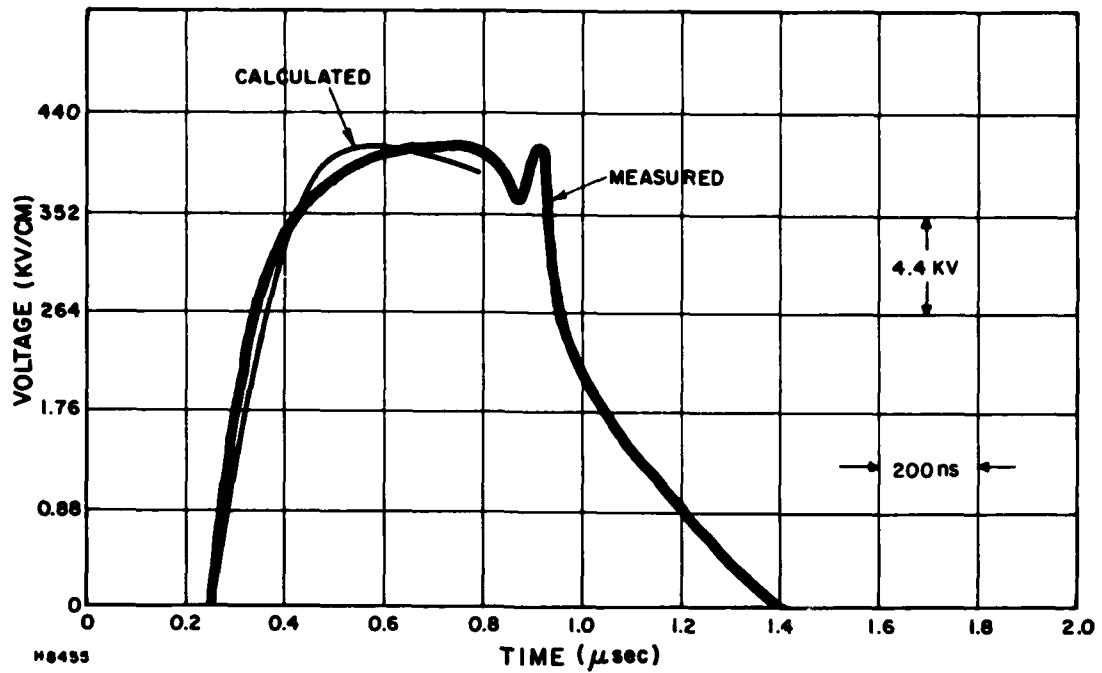


Figure 5. Comparison of Calculated and Measured Discharge Voltage and Current Characteristics

D. HgCl LASER EXPERIMENTS

Experiments were carried out to study energy extraction in HgCl lasers. The purpose of these experiments was to experimentally determine whether laser energy extraction could be achieved with high efficiency and to identify the dominant causes of inefficiency (e.g., absorption, bottleneaking) so that remedies and optimum operating regimes could be chosen.

Laser experiments were performed in the discharge regime around where the strongest HgCl* fluorescence was observed. The best laser performance achieved is summarized in Table 3. The highest intrinsic laser efficiency observed was 3% which was a factor of 4 lower than the HgCl* formation efficiency estimated from fluorescence measurements. This indicated poor energy extraction by the laser cavity flux.

To determine the dominant cause for the low extraction efficiency, the net small-signal gain coefficient (gain minus absorption) was estimated by varying the optical cavity output coupling and the length of the gain region until laser action ceased. The length of the gain region was varied by changing the discharge length along the optical axis. For the optimum lasing conditions, the net small-signal gain was estimated to be between 3.2% and 3.6%/cm.

Furthermore, the optimum output coupling was found to be close to 80%. If we then use the theory of energy extraction

TABLE 3. DISCHARGE PUMPED HgCl LASER PERFORMANCE

Intrinsic Laser Efficiency	3%
Specific Energy	1.4 J/liter (200 ns)
Discharge Enhancement Ratio	11
Laser Characteristics	
Gas Mixture	0.4% Cl ₂ /1% Hg/98.6% Ar
Total Density	2.3 amagats
E-Beam Current Density	0.6 A/cm ²
Discharge Electric Field	3 kV/cm
Discharge Current Density	70 A/cm ²

with distributed loss developed by Mangano,⁽¹⁶⁾ we can estimate the magnitude of the active medium absorption. In Figure 6 we show the calculated optimum output coupling vs g_0L , the small-signal gain per pass, with αL , the absorption loss per pass, as a parameter. The experimentally determined optimum output coupling of 80% implied an α of $> 0.5\%/cm$.

Absorption of this magnitude should be easily observable. Therefore, an experiment was undertaken to measure the absorption directly. The experimental arrangement used is shown schematically in Figure 7. A flashlamp pumped dye laser operating at 545 nm was used to probe the active medium. The wavelength was chosen to be near the HgCl laser wavelength but slightly offset to the blue to avoid HgCl* gain contributions. Under optimum laser operating conditions the absorption coefficient was measured to be $0.8 \pm 0.2\%/cm$.

With this high absorption, the low observed laser intrinsic efficiency can be readily explained. If the net small-signal gain is taken to be $3.4\%/cm$, then $g_0 \approx 4.2\%/cm$. The calculated extraction efficiency assuming no bottlenecking is 30%. This, together with the estimated HgCl* formation efficiency of 13%, implies an intrinsic laser efficiency of $\approx 4\%$. Although the observed laser efficiency was lower, these experiments did suggest that absorption was a dominant cause for inefficiency.

(16) Mangano, J.A., Unpublished

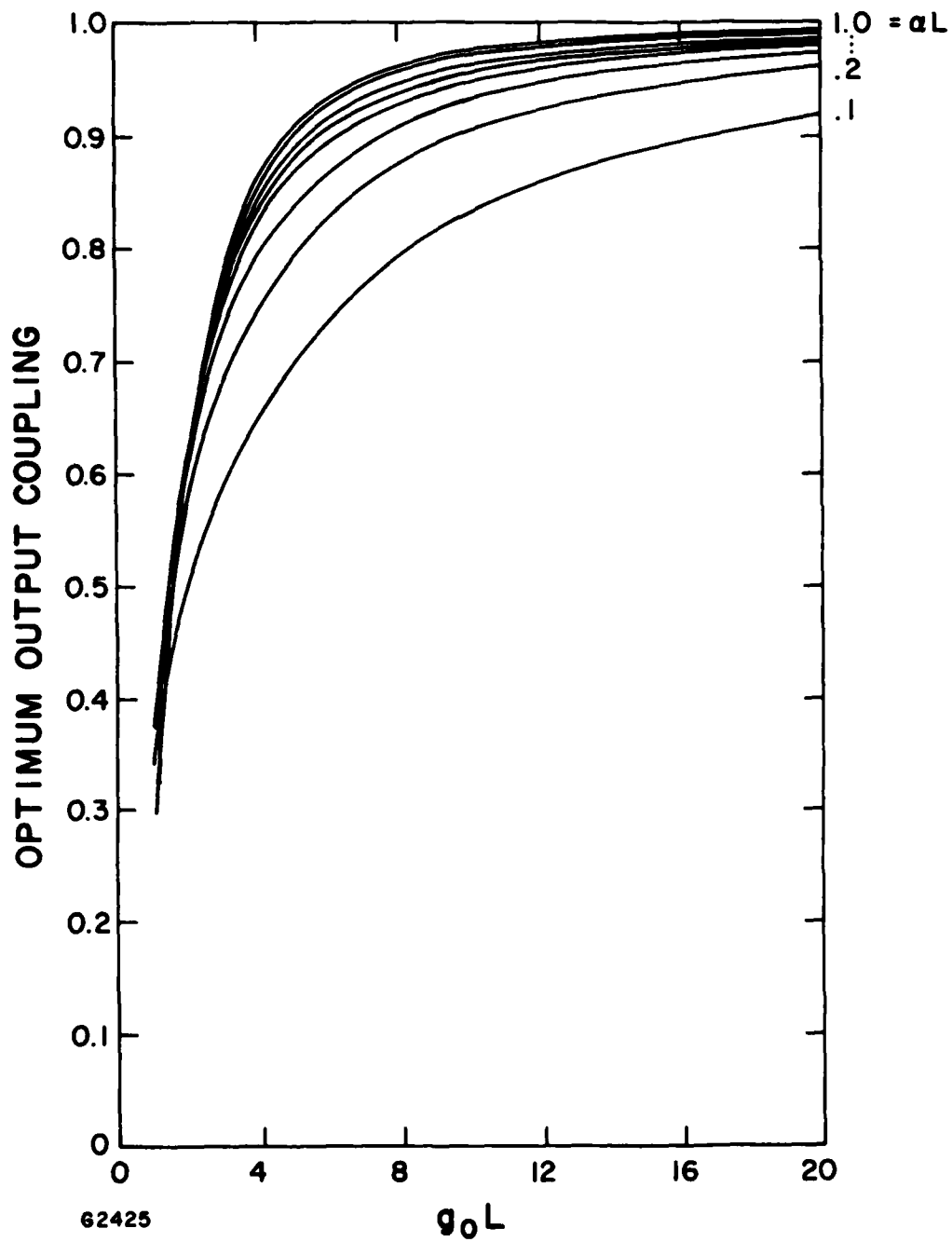


Figure 6. Optimum Output Coupling vs αL and g_0L

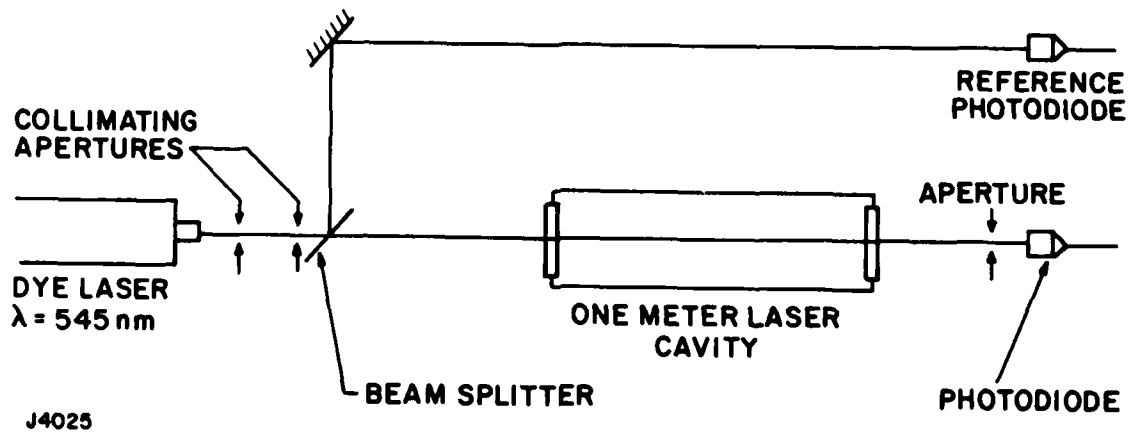


Figure 7. Active Medium Absorption Measurement Apparatus

The accuracy of these experiments was insufficient to determine whether the rate of HgCl(v = 21, 22) removal by vibrational relaxation was sufficiently fast to prevent bottlenecking. Under the discharge conditions where the small-signal gain was measured, the fluorescence intensity was measured to be $6.5 \times 10^3 \text{ W/cm}^3$. The HgCl* density can be calculated using the equation

$$\frac{n_{\text{HgCl}^*}}{\tau_s} h\nu = 6.5 \times 10^3 = P_f. \quad (7)$$

The stimulated emission cross section for HgCl* can be estimated from the emission spectra using

$$\sigma_s \tau_s = \frac{\lambda^4}{8\pi c \Delta\lambda} \approx 2.56 \times 10^{-24} \text{ cm}^2 \text{ s} \quad (8)$$

where $\Delta\lambda$ was measured to be $\sim 500 \text{ \AA}$.⁽¹⁷⁾ The small-signal gain assuming infinitely fast lower state removal is then given by

$$g_0 = \sigma_s n_{\text{HgCl}^*} = \frac{P_f}{h\nu} \tau_s \sigma_s = 5.3\%/\text{cm} \quad (9)$$

which compares with the measured value of $\approx 4.2\%/\text{cm}$. This discrepancy is within the uncertainty of the measurement.

(17) Mandl, A., Private Communication

E. CONCLUSIONS

The major findings of the HgCl* experiments can be summarized as follows:

Stable e-beam controlled discharges can be maintained in mixtures of Ar/Hg/Cl₂ at discharge power densities $> 10^5$ W/cm³ with discharge enhancement ratios > 10 . Under these discharge conditions the Hg*(³P) production efficiency was calculated to be $\approx 90\%$.

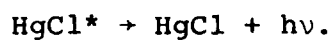
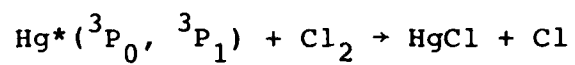
The HgCl* production efficiency deduced from absolute fluorescence intensity measurements and known or estimated quenching rate constants was $\approx 13\%$. This HgCl* production efficiency was consistent with the Hg*(³P) production efficiency only if we assumed that reactions of Hg*(³P₀, ³P₁) states with Cl₂ did not produce HgCl*. Currently small-scale experiments are underway to measure this branching ratio directly.

The highest intrinsic laser efficiency achieved was 3%. We attribute this low efficiency to inefficient energy extraction by the laser cavity flux due to high active medium absorption. The absorption was measured directly near the laser wavelength and the magnitude of the absorption was found to be sufficient to account for the observed extraction efficiency.

The dominant absorbing species have not been identified. Recently Krauss⁽¹⁸⁾ suggested the possibility of absorption from the ground HgCl (X²Σ) state to the dissociative HgCl (A²π) state.

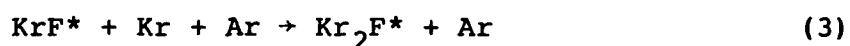
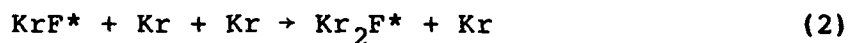
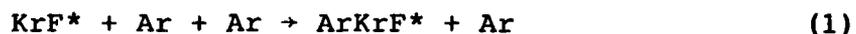
(18) Krauss, M., Private Communication

The absorption was expected to be broadband and for the low vibrational states of HgCl absorption was expected to peak near the HgCl laser wavelength. For the laser conditions described, ground state HgCl was expected to be generated in abundance via:



III. IMPROVEMENT IN KrF LASER PERFORMANCE AT ELEVATED TEMPERATURES

In typical Ar-diluted KrF laser mixtures the following reactions have been shown to be important KrF* quenching processes:



The rate constants for these have been measured⁽¹⁹⁻²¹⁾ at room temperature. These reactions also result in the formation of Kr₂F* which absorb at the laser wavelength.^(22,23) More recently Shui⁽⁵⁾ calculated the rate constants for reactions 1 and 2 theoretically and showed that they decrease dramatically at elevated temperatures. A decrease in these rate constants should lead to (a) increased KrF* fluorescence efficiency, (b) decreased Kr₂F* fluorescence and (c) improved KrF laser efficiency particularly at high (> 1 atm) pressures. In this section we report the measurement of KrF* and Kr₂F* fluorescence and KrF laser

(19) Mangano, J.A., et al., Appl. Phys. Lett. 31, 26 (1977).

(20) Jacob, J.H., et al., Appl. Phys. Lett. 33, 109 (1978).

(21) Rokni, M., et al., Phys. Rev. 16A, 2216 (1977).

(22) Stevens, W.J., Gardner, M. and Karo, A., J. Chem. Phys., 67, 2860 (1977).

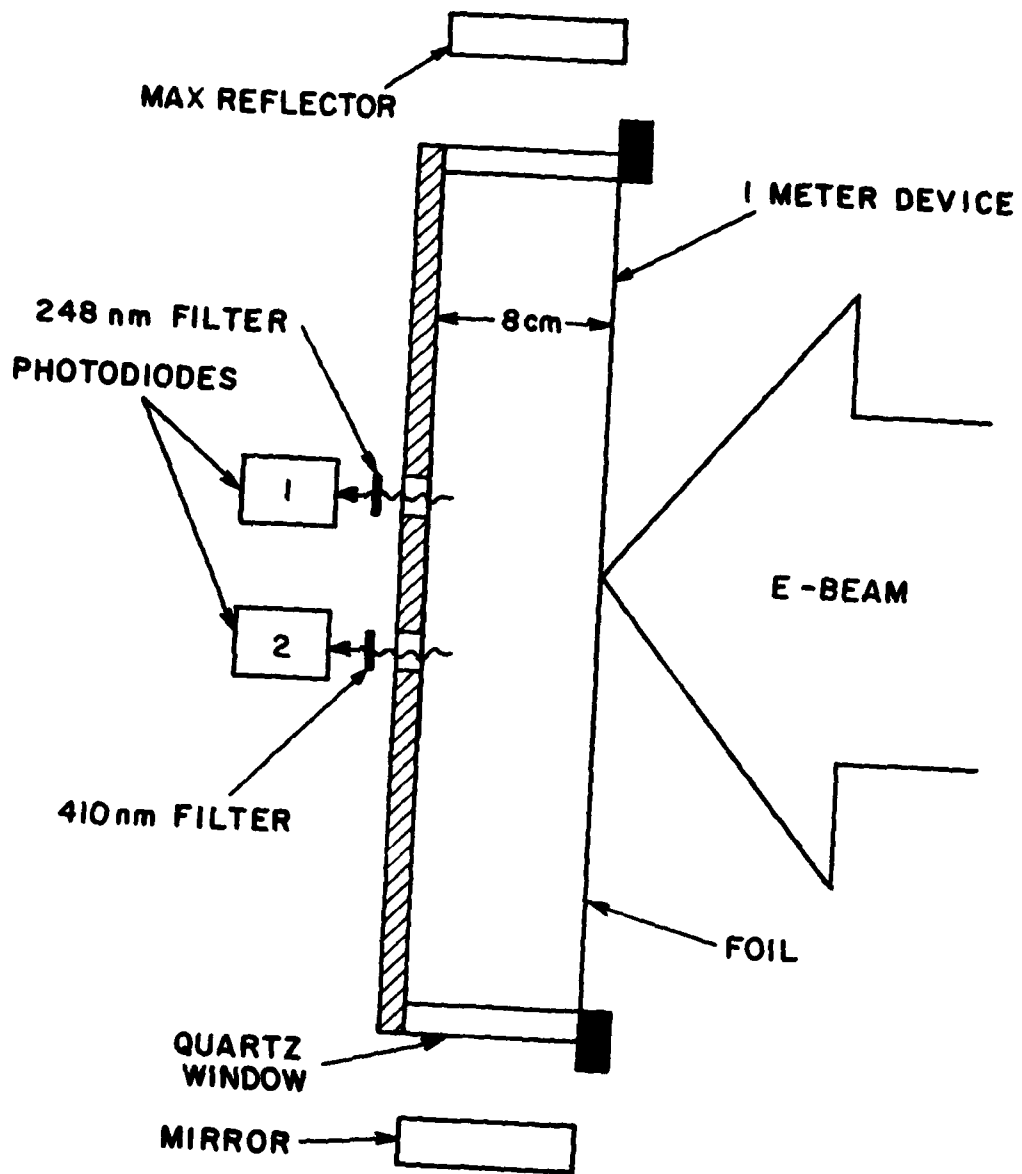
(23) Wadt, W.R., Cartwright, D.C. and Cowen, J.S., Appl. Phys. Lett., 31, 672 (1977)

efficiency as functions of temperature. The results are compared with model predictions made using the calculated temperature dependence of the rate constants. Also included is a calculated laser efficiency vs temperature scaling may for various densities.

The measurements were carried out on the one meter e-beam device which has been described previously. Relative KrF* and Kr₂F* fluorescence intensities were monitored, through side ports on the laser cavity, with S-5 planar photodiodes. A thin film bandpass filter ($\lambda_{\text{max}} = 250 \text{ nm}$, 5 nm FWHM) and a Corning glass color filter C.S. 5-260 were used to isolate the KrF* and Kr₂F* fluorescences, respectively. The arrangement is shown schematically in Figure 8. The heated laser cell and methods of output power measurement have been described previously. (7,24)

Relative steady-state KrF* and Kr₂F* fluorescence intensities were measured at various gas densities for fixed e-beam excitation intensities as functions of initial gas temperature. Data for 1.5 amagat of typical laser mixture, 0.2% F₂/4% Kr/95.8% Ar, are plotted in Figure 9. The relative laser output energy for these conditions are plotted in Figure 10. For these measurements an optical cavity with 60% output coupling was used. This output coupling was found to be approximately optimal for these laser operating conditions. The data shown in Figures 9 and 10 have been normalized to room temperature data.

(24) Mangano, J.A., et al., "One Meter KrF Laser System," Semi-Annual Report, 23 Aug. 1976 to 22 Feb. 1977.



G9665-2

Figure 8. KrF^* and Kr_2F^* Fluorescence Measurement Apparatus

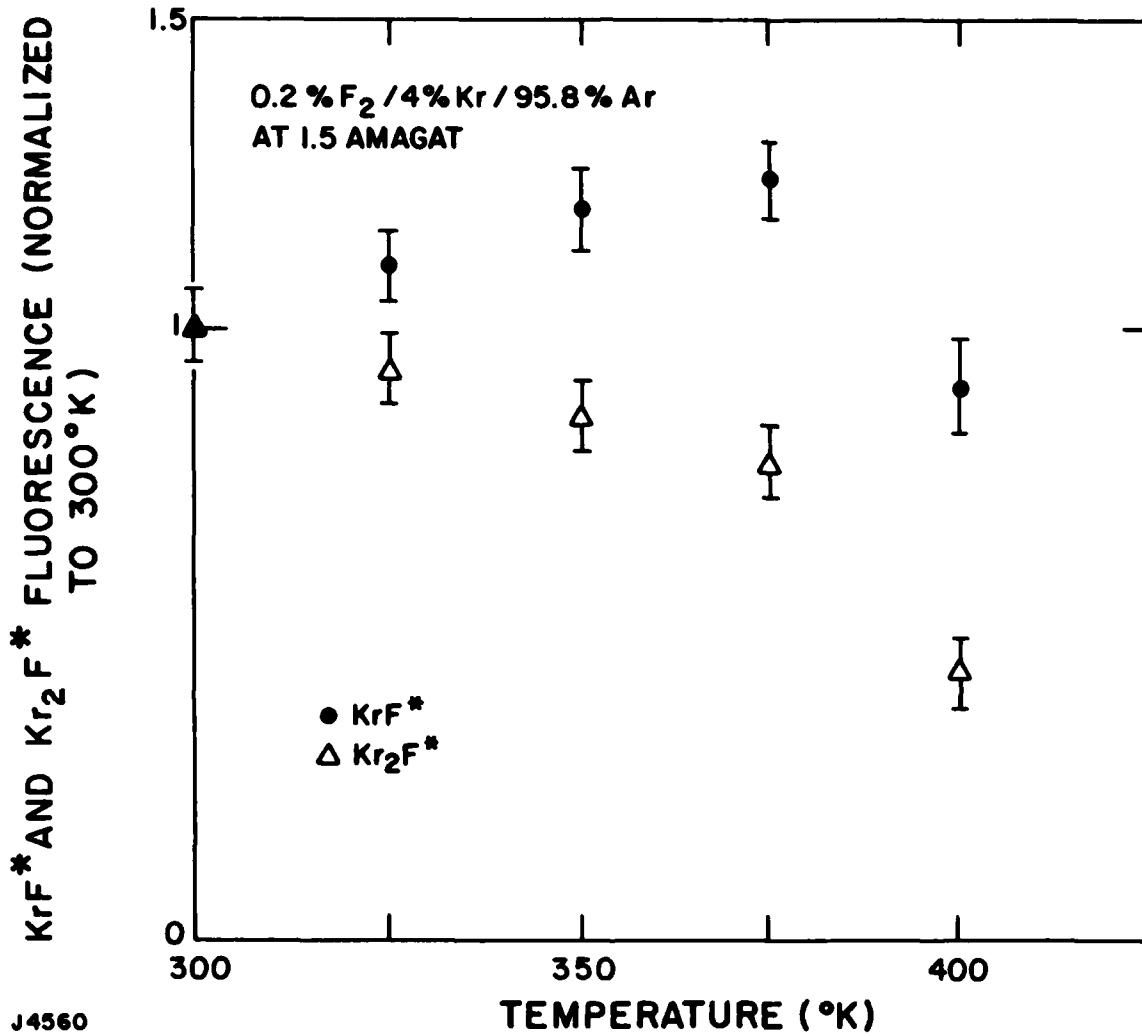


Figure 9. KrF* and Kr₂F* Fluorescence Intensity vs Temperature

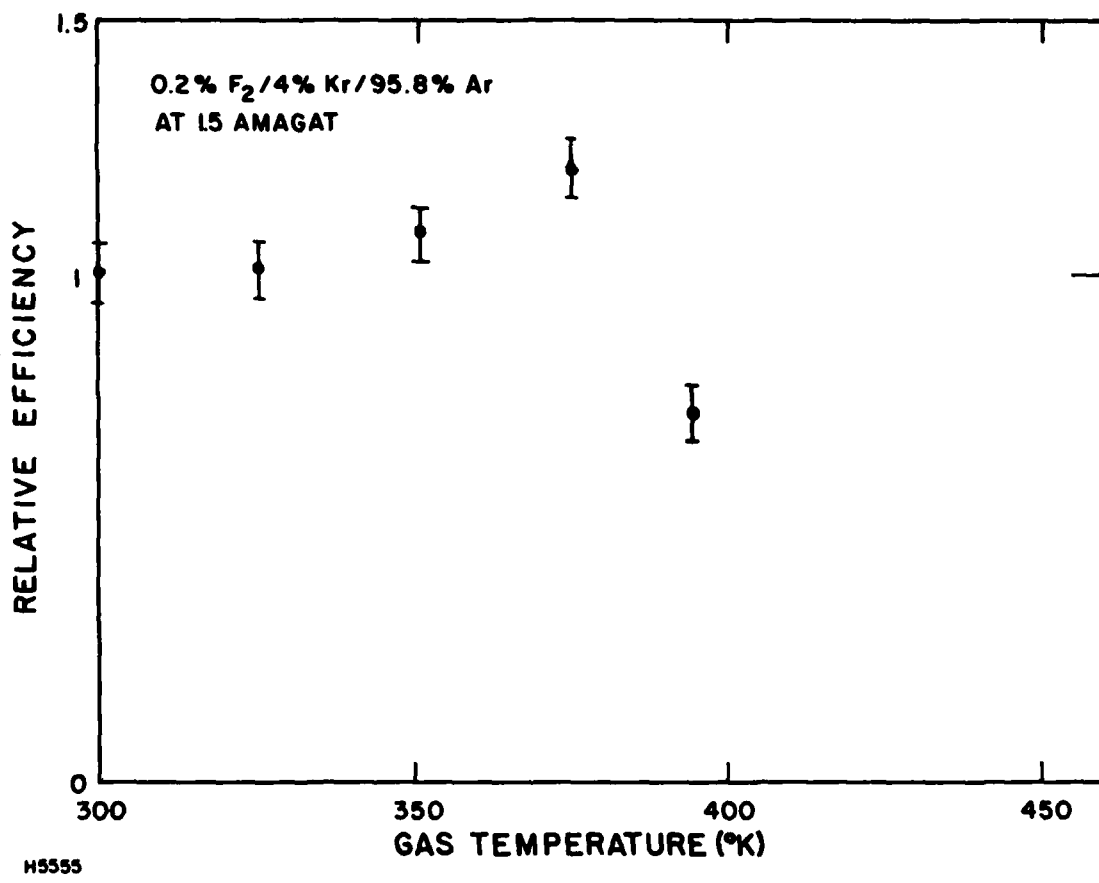


Figure 10. KrF* Laser Efficiency vs Temperature

For typical laser mixtures at density ≥ 1 amagat, the dominant quenching reactions are two body by F_2 , three body by Kr with Ar as the third body, and three body by Ar. Therefore, for excitation pulselengths long compared with KrF^* formation and quenching times, the steady-state fluorescence intensity I_{fl} can be written

$$I_{fl} = C \frac{S\tau_s}{\left(\frac{1}{\tau_s} + k_{F_2} N_{F_2} + k_{2Ar} N_{Ar}^2 + k_{ArKr} N_{Kr} N_{Ar}\right)} \quad (10)$$

where τ_s is the spontaneous lifetime of KrF^* , k_{F_2} , k_{2Ar} and k_{ArKr} are the quenching rate constants for two-body quenching by F_2 , three-body quenching by Ar, and Kr with Ar as the third body, respectively. N_{F_2} , N_{Ar} and N_{Kr} are densities of F_2 , Ar and Kr.

One can compare the measured temperature variation of KrF^* fluorescence intensity with that one expects to find by: (1) using the measured room temperature rate constants given in Table 4, (2) assume that k_{F_2} does not depend on temperature, (3) assume that $k_{ArKr} \approx k_{2Kr}$ and (4) normalizing the calculated k_{2Ar} and k_{2Kr} at room temperature to that measured. With these assumptions the temperature dependence of KrF^* fluorescence predicted using Eq. (10) is plotted in Figure 11.

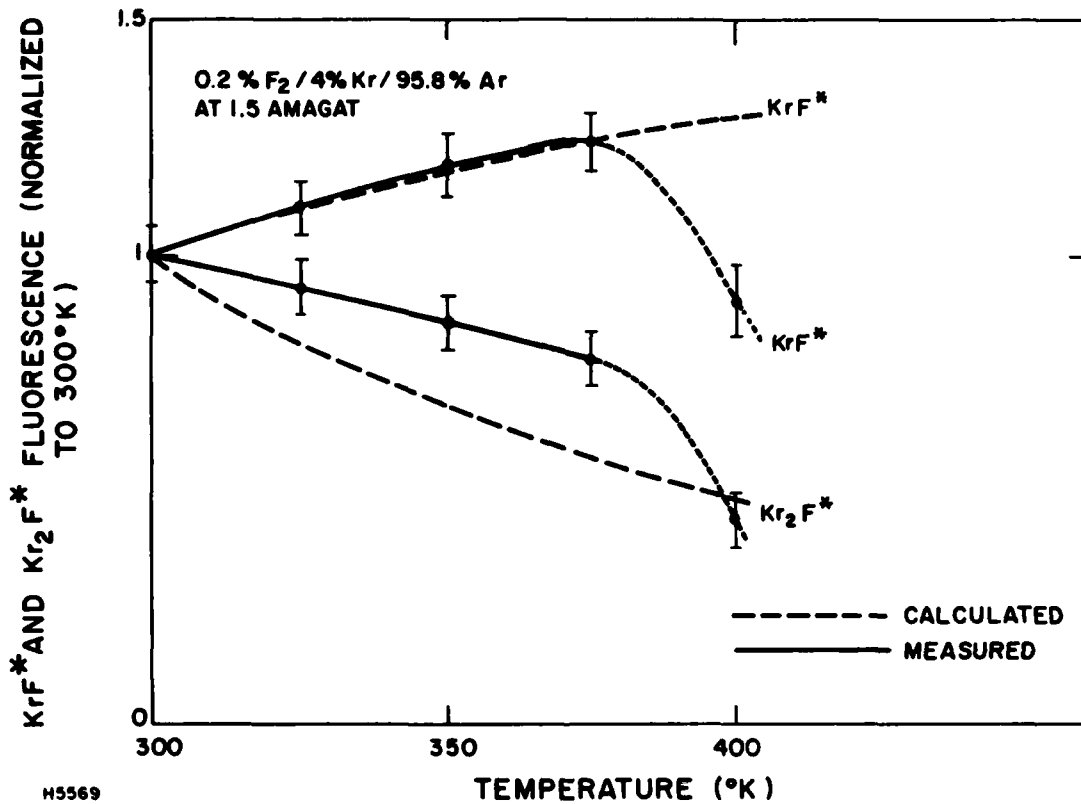
Kr_2F^* is predominantly formed in e-beam excited KrF laser mixtures by reaction (3) and by (1) followed by



If the quenching rate for Kr_2F^* is assumed to be temperature insensitive, then the temperature dependence of Kr_2F^* fluorescence intensity can be calculated. This is shown also in Figure 11.

TABLE 4. KrF* QUENCHING RATE CONSTANTS

<u>Reaction</u>	<u>$k\tau_s$</u>	<u>$k (\tau_s = 6.5 \mu s)$</u>
KrF* + F ₂ → Products	5 x 10 ⁻¹⁸ cm ³	7.8 x 10 ⁻¹⁰ cm ³ /s
KrF* + 2 Kr → Kr ₂ F* + Kr	4.4 x 10 ⁻³⁹ cm ⁶	6.7 x 10 ⁻³¹ cm ⁶ /s
KrF* + Kr + Ar → Kr ₂ F* + Ar	4.2 x 10 ⁻³⁹ cm ⁶	6.5 x 10 ⁻³¹ cm ⁶ /s
KrF* + 2 Ar → Products	4.6 x 10 ⁻⁴⁰ cm ⁶	7 x 10 ⁻³² cm ⁶ /s



H5569

Figure 11. Calculated and Measured KrF* and Kr₂F* Fluorescence Intensities vs Temperature

Note that the comparison between predicted and measured KrF* fluorescence intensities show good agreement for temperature lower than 375°K. At higher temperatures the measured fluorescence decreased with temperature, while the predicted fluorescence continued to increase. Subsequently it was determined by spectroscopic means that at temperatures > 375°K substantial prereaction occurred between F₂ used in the laser mixture and the teflon-coated cell walls prior to excitation by the e-beam. This can explain the discrepancy between the predicted and observed KrF* fluorescence intensities at the higher temperatures.

The observed decrease in Kr₂F* fluorescence intensity with increasing temperature is smaller than that predicted. This is probably due to a decrease in Kr₂F* quenching with temperature.

Incorporating the calculated temperature dependent KrF* quenching rate constants into the laser model, described in detail previously, ⁽⁷⁾ one can also predict laser performance as a function of temperature. The calculated laser output intensity vs temperature is shown in Figure 12. Note that good agreement has been obtained up to the temperature where F₂ prereaction became a problem.

Because three-body quenching increases as the square of the gas density, the effect of reduced quenching is expected to be more pronounced at higher densities. In Figure 13 we have used the laser model to project laser intrinsic efficiency (laser energy out/e-beam energy deposited) achievable at various densities

Kr F* LASER EFFICIENCY vs TEMPERATURE

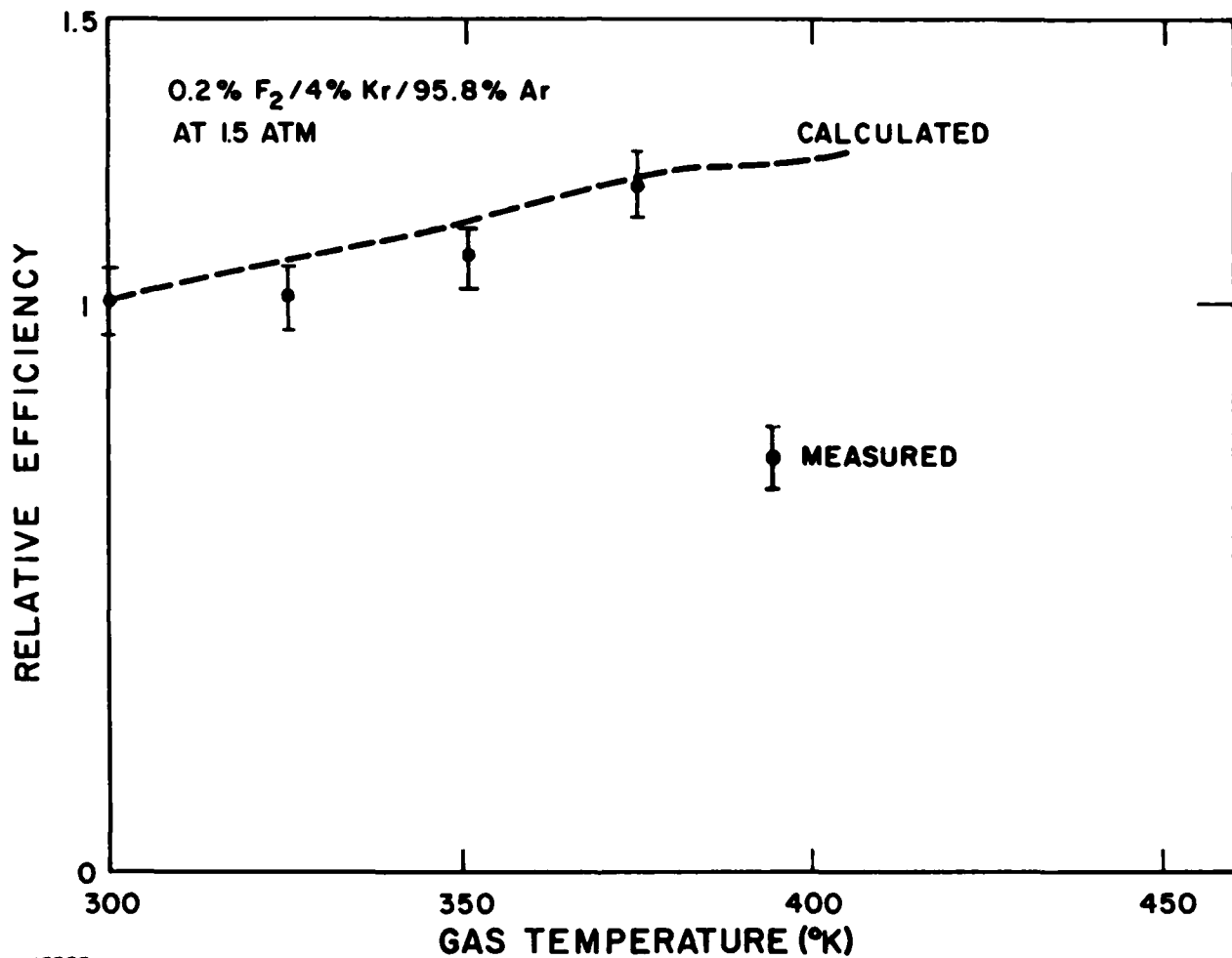


Figure 12. Calculated and Measured Laser Output Energy vs Temperature

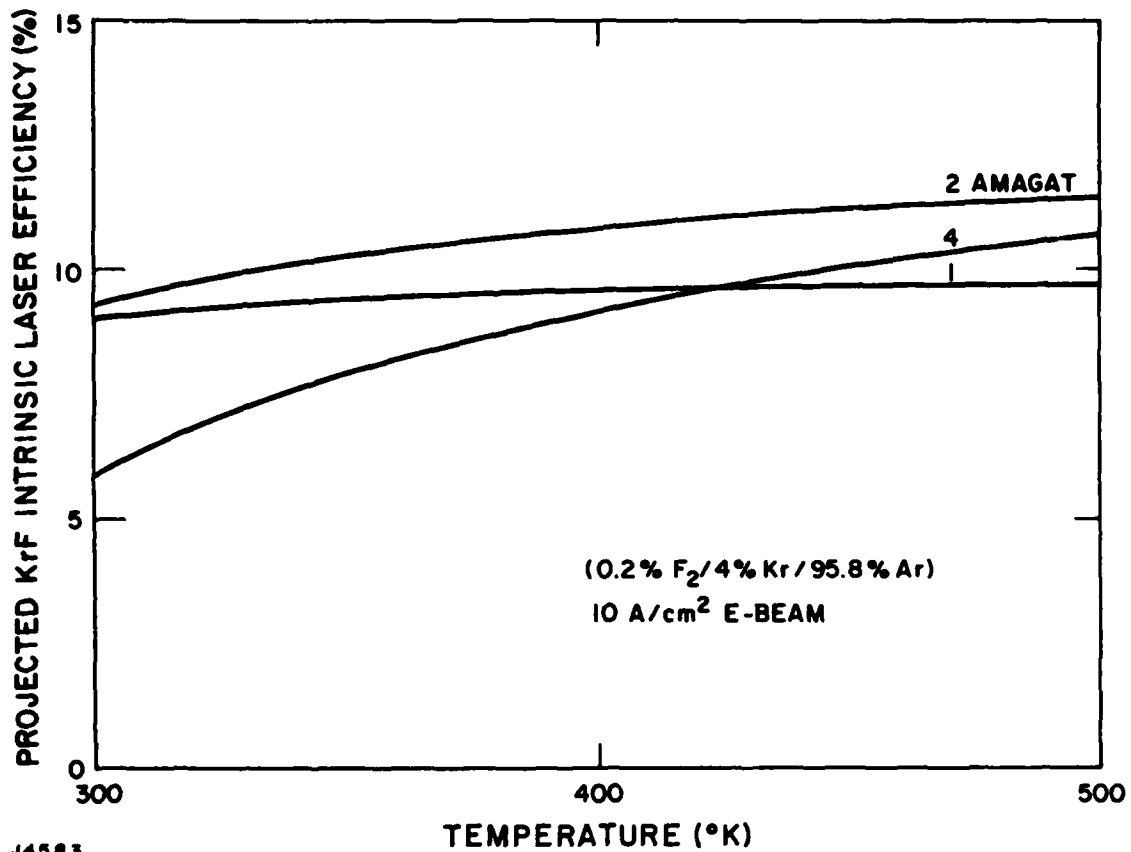


Figure 13. Projected KrF Laser Efficiency vs Temperature at Various Gas Densities

and temperatures. For these calculations we have assumed a one-meter long active volume laser with a 300 kV incident e-beam with current density of 10 A/cm^2 .

In conclusion, we have measured relative KrF^* fluorescence efficiency in e-beam excited KrF laser mixtures as a function of temperature. In the range 300°K to 375°K the measurements are consistent with reduced three-body KrF^* quenching by Ar and Kr predicted by Shui. We have also demonstrated improved KrF laser performance and show that this improvement can be attributed to reduced KrF^* quenching. The measured decrease in Kr_2F^* density is less than that predicted assuming constant Kr_2F^* quenching. We attribute this discrepancy to reduced Kr_2F^* quenching at elevated temperatures. The calculated variation in KrF^* quenching rate constants with temperature have been incorporated into a comprehensive laser model and predictions of pressure scaling of KrF laser performance have been made.

IV. XeF LASER EXPERIMENTS

In the previous reporting period we demonstrated an XeF intrinsic laser efficiency of 5.5% by heating the laser mixture to elevated temperatures prior to e-beam excitation. The improvement in efficiency over that achieved at room temperature was shown to be due to improved energy extraction by the laser cavity flux. The highest specific energy achieved was 2.5 J/liter amagat. This specific energy was limited by our e-gun pulse energy rather than intrinsic laser processes.

The limit on e-gun pulse energy delivered to the laser gas mixture was imposed by diode closure in the e-gun. Quantitatively, the diode characteristics can be approximated by the Langmuir-Child space-charge limited current with a time dependent anode-cathode spacing:

$$J_{eb} = 2.3 \times 10^{-6} \frac{V^{3/2}}{(d - V_c t)^2} \quad (11)$$

where J_{eb} is the current density in A/cm^2 in the e-gun, V is the e-gun voltage, d is the physical anode-cathode spacing in cm, V_c is the closure velocity in cm/s and t is the time after turn-on. At constant gun voltage, diode closure gives a constantly increasing current density in the gun.

For optimum laser performance the current density impinging on the laser mixture must be kept within the range 7 to 20 A/cm^2 .

Below this range the medium is not sufficiently inverted to allow efficient energy extraction and above this range rapid electron quenching of the upper laser state prevents efficient laser operation. The specific pulse energy per cm^3 delivered to the laser mixture is given by

$$E = f \text{ Sp } \int_0^\tau J_{\text{eb}} dt = 2.33 \times 10^{-6} f \text{ Sp } \frac{V^{3/2}}{V_c d} [\sqrt{F} - 1] \quad (12)$$

where f is the transmission of the anode screen, foil, and foil support structure, Sp is the stopping power of the laser mixture, τ is the pulselength, and F is the ratio of final e-beam current to initial e-beam current.

Equation (12) can also be written as

$$E = (2.33 \times 10^{-6} f J_{\text{cav}}(0))^{1/2} \frac{V^{3/2}}{V_c} (\sqrt{F} - 1) \text{ Sp} \quad (13)$$

where $J_{\text{cav}}(0)$ is the initial current density in the laser cavity. Equation (13) can be used to estimate the maximum pulse energy deliverable to the laser gas in the one meter device. We have $V_c \sim 2.3 \text{ cm}/\mu\text{s}$ (tantalum blade cathode), $F \approx 0.5$ and $V = 250 \text{ kV}$. The average stopping power with neon in the cavity is $\sim 5.5 \text{ kV}/\text{cm-amagat}$. If we allow the cavity current to vary between $7 \text{ A}/\text{cm}^2$ and $21 \text{ A}/\text{cm}^2$, then $F = 3$. With the above values, Eq. (13) gives

$$E = 5.6 \times 10^{-2} \text{ J}/\text{cm}^3\text{-amagat} = 56 \text{ J}/\text{liter-amagat}.$$

At an intrinsic laser efficiency of 5.5% this energy input limit would imply that the maximum specific energy achievable was $3.1 \text{ J}/\text{liter-amagat}$.

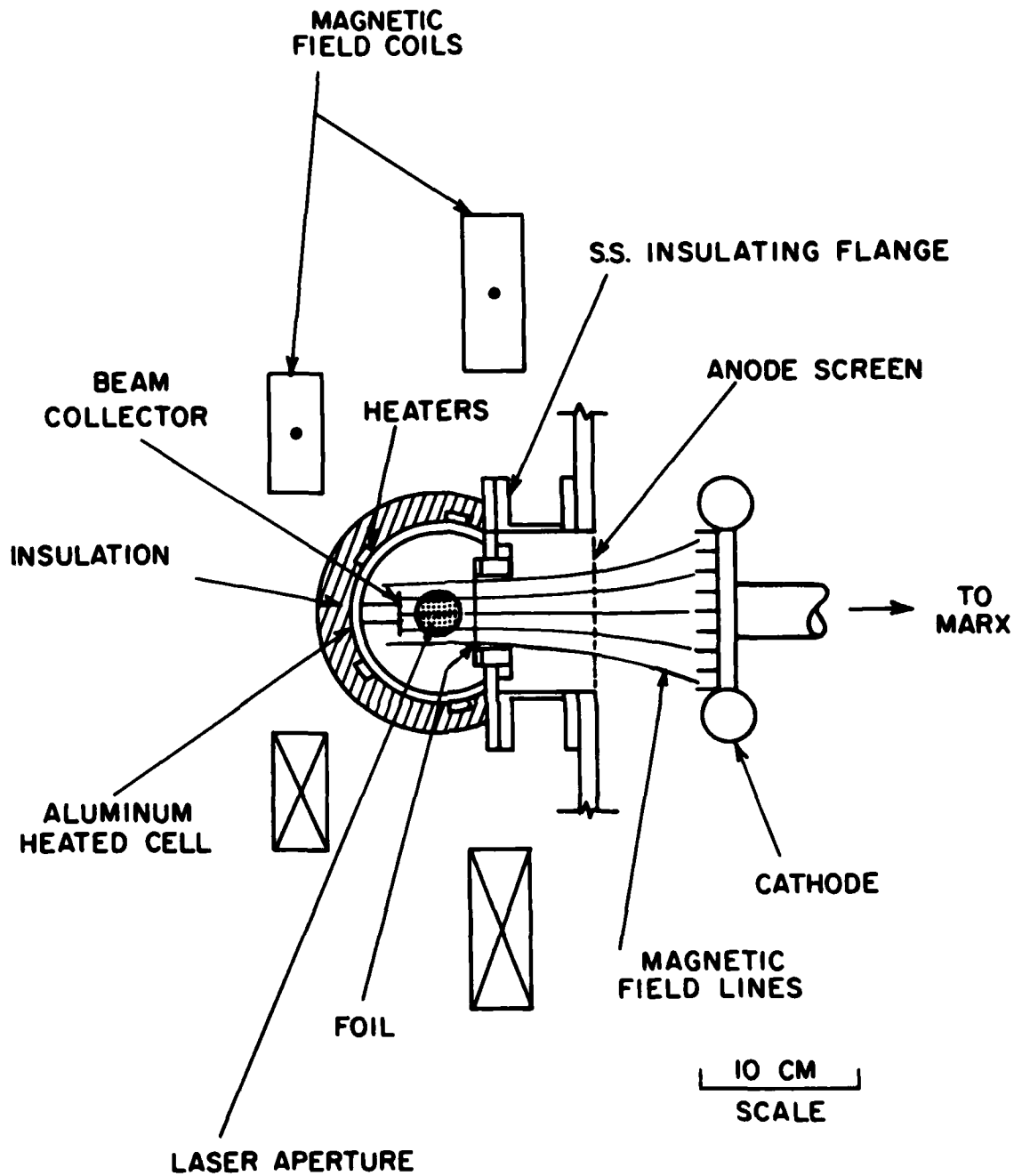
In previous XeF laser experiments the maximum useful energy delivered to the laser mixture was 45 J/liter-amagat. This was slightly lower than that calculated above principally because the circuit inductance in the Marx generator limited the risetime of the voltage to ≈ 200 ns. The specific laser energy achieved was 2.5 J/liter-amagat. Analysis of the laser output pulse-shape indicated that higher specific energies should be possible if the input pulse energy was increased.

A convenient method of partially circumventing the diode closure energy constraint is by using magnetic field compression of the e-beam to increase the current density after it emerged from the diode region. From Eq. (13) it is clear that for a compression ratio of R, the specific e-beam pulse energy is given by

$$E = (2.33 \times 10^{-6} f R J_{\text{cav}}(0))^{1/2} \frac{v^{3/4}}{v_c} (\sqrt{F} - 1) \text{ Sp} \quad (14)$$

To demonstrate higher XeF specific energy using the one meter device a compression ratio of 2.5 was chosen. This was the highest practical compression ratio that could be used while still yielding sufficient height in the resultant beam to allow uniform energy deposition within the 2.5 cm diameter laser aperture. A scaled drawing of a cross section of the e-gun and laser cell showing the size and location of the field coils is shown in Figure 14.

A smaller field coil than those used previously was constructed in order to produce the rapidly converging magnetic field required to compress the e-beam by a factor of 2.5 in the e-gun



J4161

Figure 14. Cross Section of the Small Aluminum Heated Cell

and in order to comply with the maximum power capability of the existing power supplies. An existing small, 0.6 liter active volume aluminum cell was adapted to the e-gun for these experiments because of the space limitations imposed by the magnetic field coils. The position of the field coils and the e-beam drift region was chosen so that the resultant maximum magnetic field was 600 g at the surface of the cathode and 1.5 kg at the plane of the foil. The spacing of the coils was chosen to yield an approximately uniform field within the active laser volume.

The inner surface of the cell was coated with a high temperature Teflon coating for high temperature fluorine compatibility. This coating was quoted by the manufacturer to be capable of continuous service up to 500°F. The coating used in the XeF experiments reported previously was coated with a Teflon coating rated for up to 450°F. In the previous experiments the laser efficiency was found to decrease for temperatures higher than 470°K. It was suggested that a possible reason for the decrease was that at the higher temperatures the coating introduced appreciable amounts of impurities into the laser mixture to adversely affect laser operation. If this was the case, then one would expect the efficiency to fall off at a higher temperature with the present cell.

The intrinsic laser efficiency was therefore remeasured at various temperatures. The results obtained at 3 amagats are shown in Figure 15. For comparison, the previously reported results are also plotted. Note that the comparison shows that the present data do exhibit a later efficiency decrease. This strongly suggests

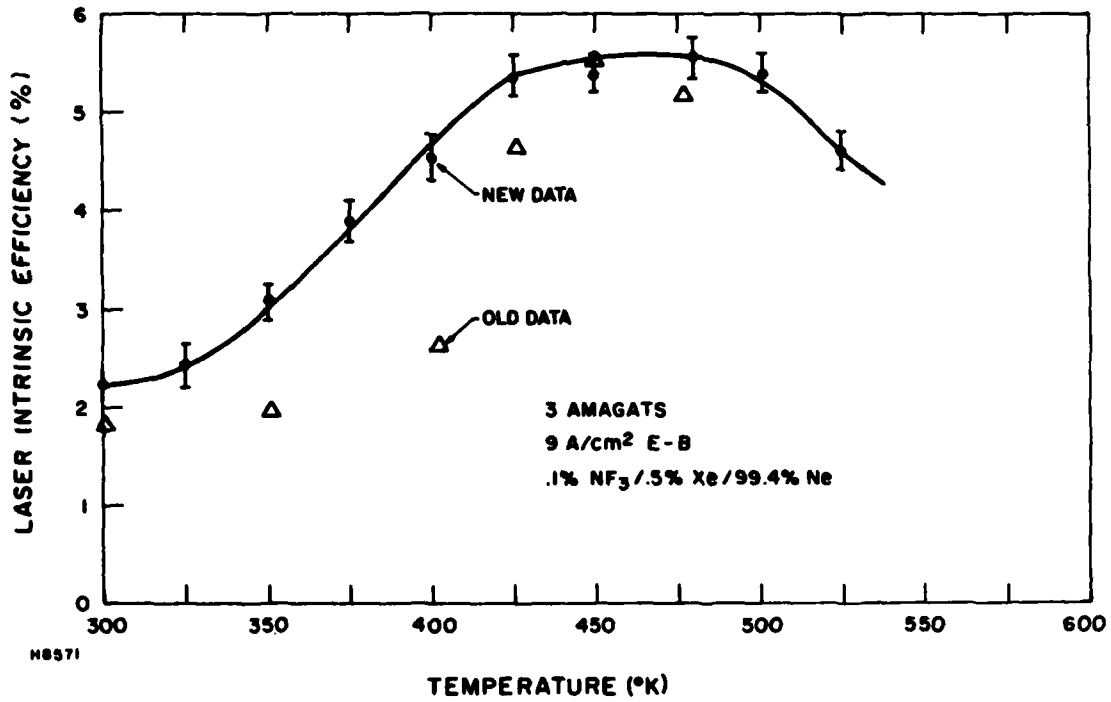


Figure 15. Measured Intrinsic Laser Efficiency at Various Temperatures

that the high temperature falloff in efficiency was at least partially due to cell related effects. It is very likely that in the present cell the efficiency decrease at temperature $> 500^{\circ}\text{K}$ is also cell related, rather than due to some fundamental process in the laser mixture. This will be resolved in future experiments which will be carried out in an all stainless steel cell.

It is interesting to note that, since Figure 15 shows the measured intrinsic laser efficiency as a function of initial gas mixture temperature, and since measurements were taken with a constant pulse energy input of 35 J/liter-amagat, the final mixture temperature was some 60°K higher. In Figure 16 we plotted the efficiency as functions of both initial and final temperatures. Note that Figure 16 implies that the intrinsic efficiency remained above 5% for the temperature range 410° to 560°K . If the observed efficiency falloff was due entirely to some unavoidable temperature related process, then if one operates the laser with an initial temperature of 410°K and allows the temperature to rise to 570°K during the pulse, the average efficiency can be expected to remain $> 5\%$. This would imply a specific energy of 4.6 J/liter-amagat.

The e-beam energy deposition in the active laser volume with e-beam compression was then measured. The measurement was made with an aluminum plate calorimeter shown schematically in Figure 17. The active surface of the calorimeter was 2.5 cm along the height by 10 cm along the length of the e-beam. The active calorimeter surface was first placed at the edge of the active laser

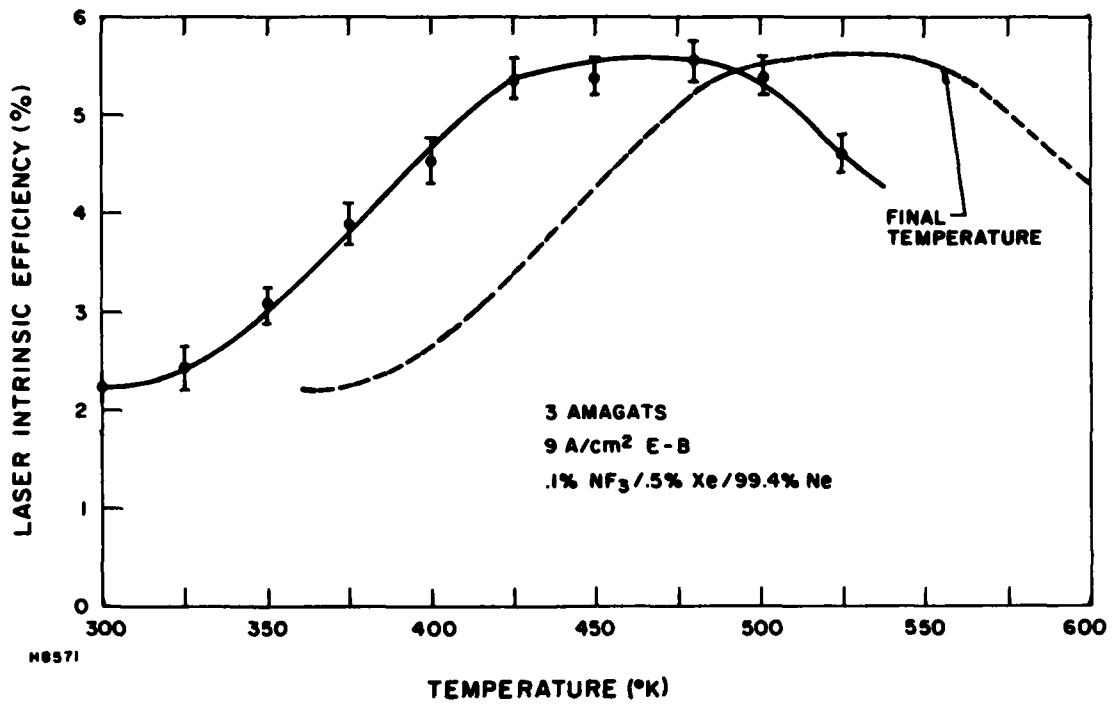


Figure 16. Measured Intrinsic Laser Efficiency vs Initial and Final Temperatures

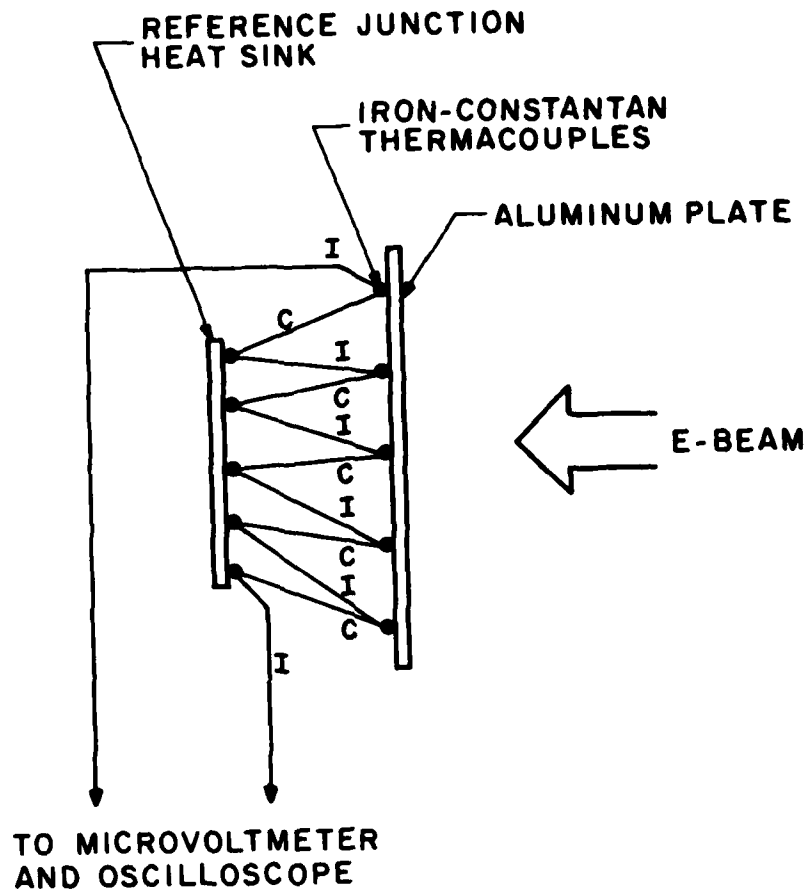


Figure 17. E-Beam Calorimeter

volume closest to the foil with 3 amagats of laser mixture in the cavity. The e-beam energy deposited in the calorimeter was measured by recording the temperature change after the e-beam pulse. The measurement was then repeated at the downstream edge of the active volume. The difference between the measurements, corrected for e-beam energy reflected ($\approx 10\%$), was then taken as the energy deposited in the active volume. This method was used because the active laser volume was small compared with the total cell volume irradiated by the e-beam and the time/spatial variation in deposition made energy deposition via pressure rise measurements invalid.

The energy deposited in the active volume with a $1.7 \mu\text{s}$ e-beam pulselength was $285 \pm 30 \text{ J/liter}$ at 3 amagats which corresponded to $95 \text{ J/liter-amagat}$. This was larger than that one would calculate using Eq. (13). The reason for this was that the voltage droop in Marx bank coupled with space charge in the e-beam drift region limited the transmitted e-beam current density in the cavity so that a longer pulselength could be used.

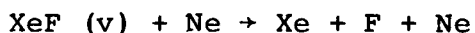
With this energy input a laser energy of 7 J was extracted in a 2.54 cm diameter by 100 cm long active laser volume which corresponded to a specific energy of 14 J/liter or $4.67 \text{ J/liter-amagat}$. The laser mixture consisted of 0.15% NF_3 /0.5% Xe/99.35% Ne at 3 amagats. The initial gas temperature was 425°K . The corresponding intrinsic laser efficiency was $5 \pm 0.5\%$. The uncertainty in the efficiency was due to the $\pm 10\%$ uncertainty in the e-beam energy deposition.

V. RATE CONSTANTS FOR GROUND STATE DEACTIVATION

A. INTRODUCTION

XeF is one of the two rare gas halides which has an appreciably bound ground state. As a result, the XeF laser transitions are bound-bound rather than bound-free, as is the case for all other rare gas halides except XeCl. The XeF laser transitions are indicated in Figure 18. It can be seen from this figure that the lower lasing levels lie $\sim 400-700 \text{ cm}^{-1}$ below the dissociation limit which is sufficient to cause noticeable bottlenecking, especially at room temperature.

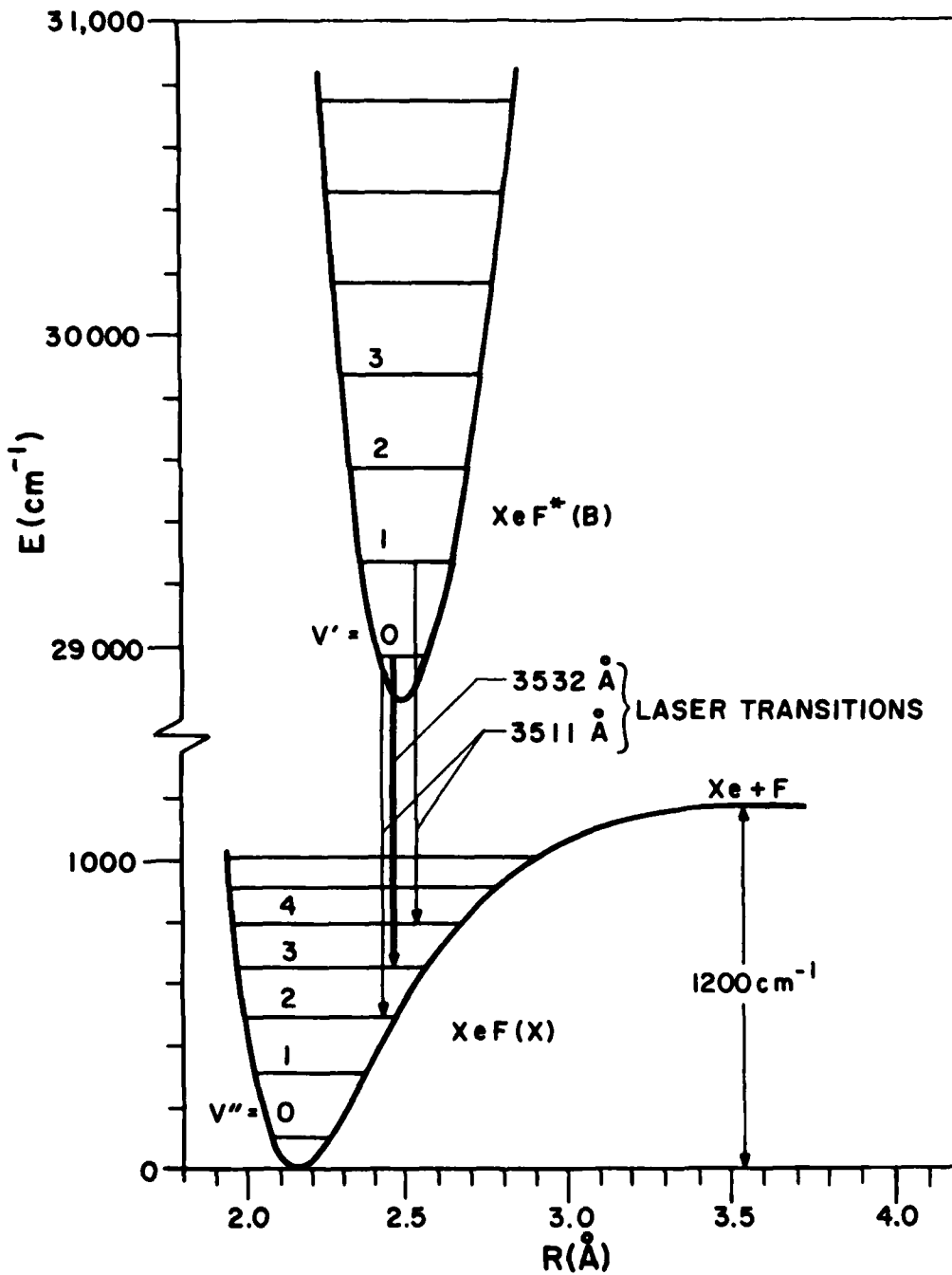
One part of this program involved the calculation of rate constants for the ground electronic state of XeF for the reactions



and



The rate constants were calculated for several different rotational distributions and incorporated into the ground state master equation which was then used to determine whether the bottlenecking predicted using these rate constants was sufficient to explain the experimentally observed laser behavior.



H1990

Figure 18. Potential Energy Diagram for XeF Indicating the UV Lasing Transitions

In order to calculate these rare constants, a combination of phase space theory⁽²⁵⁾ and Monte Carlo trajectory calculations⁽²⁶⁾ was used. This is a well developed technique which has been used for a variety of three-body systems.⁽²⁷⁾ A description of this technique is contained in Section B, a discussion of the rate constants obtained is presented in Section C and the master equation results are given in Section D.

B. THEORY

A system of n particles, with well defined mutual interactions, can be described by a point in a $6n$ dimensional phase space whose coordinates are the conjugate momentum and position vectors of the particles. The time evolution of any configuration on these n particles can be determined by following the representative point through phase space. Since phase space contains all possible interaction configurations of the n particles, it is possible to define a surface which divides phase space into two regions, one of which contains "reactants" and the other "products." The rate of a reaction can then be defined as the one-way flow of points across the dividing surface.

$$R_s = \int_S f \rho (\vec{v} \cdot \vec{n}) dS \quad (15)$$

(25) Keck, J.C., Adv. Chem. Phys. 13, 85 (1967).

(26) Bunker, D.L., Methods Comput. Phys. 10, 287 (1971).

(27) Shui, V.H., J. Chem. Phys. 58, 4868 (1973).

where R_S is the rate of reaction, $\rho(\vec{p}, \vec{q})$ is the density of points, \vec{n} is the unit vector outward normal to dS and \vec{v} is the generalized velocity in phase space. The components of \vec{v} may be obtained from the Hamiltonian equations of motion

$$\dot{q}_i = \partial H / \partial p_i \quad \text{and} \quad \dot{p}_i = -\partial H_i / \partial q_i \quad (16)$$

where $H(\vec{p}, \vec{q})$ is the Hamiltonian of the system, f is the function which corrects for multiple passes of the same point over the surface S , which defines the surface integral. The rate coefficient, which is independent of concentration, can then be defined by

$$k_S = R_S / \Pi [M_i], \quad (17)$$

where $[M_i]$ is the concentration of species i in the initial state.

Due to the presence of the unknown function f in the integrand of Eq. (15), the expression for R_S cannot be evaluated analytically. Monte carlo methods are, therefore, used. Monte Carlo techniques allow one to randomly pick initial conditions for the system under investigation and follow the time behavior of the particles using the equations of motion, defined in Eq. (16). An estimate of the fraction of trajectories which react, and remain reacted, can thus be obtained and this information used to determine f . A more detailed

description of both the Monte Carlo techniques used in this study and phase space theory can be found in Ref. 27.

In order to solve the equations of motion used in the Monte Carlo procedure, it is necessary to know the manner in which the various particles interact. Ideally, this should be determined from a three-body potential energy surface; however, for the Xe-F-Ne system, no such surface has been calculated. To avoid this problem, we use the assumption that a three-body interaction can be approximated by the sum of the individual two-body potentials.

Information on the ground state potential of XeF is available from several sources. Smith and Kobrinsky⁽²⁸⁾ used absorption spectroscopy to determine the ground state well depth and spectroscopic constants. Tellinghuisen, et al.,⁽²⁹⁾ obtained emission spectra for the B→X and D→X transitions in XeF and applied RKR methods to this data to obtain the ground state potential curve. In addition, crossed molecular beam experiments on the Xe(¹S) + F(²P) system have been performed by Becker, et al.⁽³⁰⁾ Agreement between Refs. 29 and 30 is excellent.

For ease of computation, we have assumed that the ground state of XeF can be described with sufficient accuracy by a

(28) Smith, A.L. and Kobrinsky, P.C., J. Mol. Spect. 69, 1 (1978).

(29) Tellinghuisen, P.C., Tellinghuisen, J., Velazco, J.E., Coxon, J.A. and Setser, D.W., J. Chem. Phys. 68, 5187 (1978).

(30) Becker, C.H., Casavecchio, P. and Lee, Y.T., J. Chem. Phys. 69, 2377 (1978).

Leonard-Jones potential. A Leonard-Jones potential correctly models the behavior at large internuclear separations, but is too attractive in the region near the equilibrium separation. To determine the magnitude of the error that this assumption introduced into our results, we also ran test cases with a 12-8 potential, which more accurately models behavior near the equilibrium internuclear distance, but is too repulsive at large separations. The results using these two potentials were indistinguishable, given the statistical fluctuations in our answers.

It was assumed that the F-Ne interaction could be approximated by that of Ne-Ne. Again, a Leonard-Jones potential, using the Ne₂ ground state spectroscopic parameters of Tanaka and Yoshino,⁽³¹⁾ was assumed. The binding energy and equilibrium internuclear distance of Xe-Ne were estimated by the arithmetic mean of the Xe₂⁽³²⁾ and Ne₂⁽³¹⁾ internuclear separations and the geometric mean of the binding energies. To test the sensitivity of our results to these well depths and shapes, test cases were run using strictly repulsive potentials of the form, $V = A_i \exp(-r/L_i)$ for both F-Ne and Xe-Ne. The parameters A_i and L_i were obtained from a paper by Abrahamson.⁽³³⁾ Again, no significant differences were observed.

(31) Tanaka, Y., and Yoshino, K., J. Chem. Phys. 57, 2964 (1972).

(32) Docken, K.K. and Schafer, T.P., J. Mol. Spect. 46, 454 (1973).

(33) Abrahamson, A.A., Phys. Rev. 178, 76 (1969).

C. RATE CONSTANT RESULTS

Calculations were performed for the first six vibrational levels of XeF, both dissociative and V→T, R rate constants were obtained and three different assumptions concerning the rotational population distribution were used. These assumptions are as follows:

- (1) Boltzmann distribution to the dissociation limit
- (2) No rotational energy present (J=0)
- (3) Molecules in the most probable rotational state for 300°K (J=24)

These three sets of calculations were performed in order to test the effect of available rotational energy on the dissociative rate constants. It was felt that this effect might be large, since the bound states of interest are within several kT of the dissociation limit. Assumptions (1) and (2) place rough upper and lower bounds on our results, respectively. It has been shown that the population in states very near the dissociation limit (in our case, states with large J) is less than predicted using a Boltzmann distribution due to very rapid communication with the dissociative continuum. Using assumption (1) will, therefore, weight contributions to the dissociative rate constants from high lying J levels too heavily and, consequently, will yield values which are expected to be an upper bound on "real" values.

An alternative way of expressing assumption (2) is to state that there is no communication possible between the vibrational and rotational modes of a molecule. While this is obviously an unrealistic assumption, it should provide a lower bound for our calculations.

The third assumption was chosen to give us a representative intermediate case. There is no reason, however, to expect this assumption to yield the "real" rate constants, but unless the rotational distribution produced during lasing is extremely unusual, the constants obtained using this assumption should be the most realistic of our three sets.

The rate constants for collisional dissociation, using our three assumptions, are shown in Figure 19. In order to minimize the effect of statistical fluctuations, which are inherent in our method, our calculated rate constants were fit to an analytic expression which has been shown to accurately model a wide variety of systems.

$$k_D(v) = A \exp(-a \epsilon_v)$$

where ϵ_v is the dissociation energy in cm^{-1} . It is the fitted results that are shown in Figure 19. All values are expected to be accurate to within a factor of 2. The factor of 15 difference in the results for $v=0$ clearly demonstrates the sensitivity of our results to the exact form of the rotational distribution.

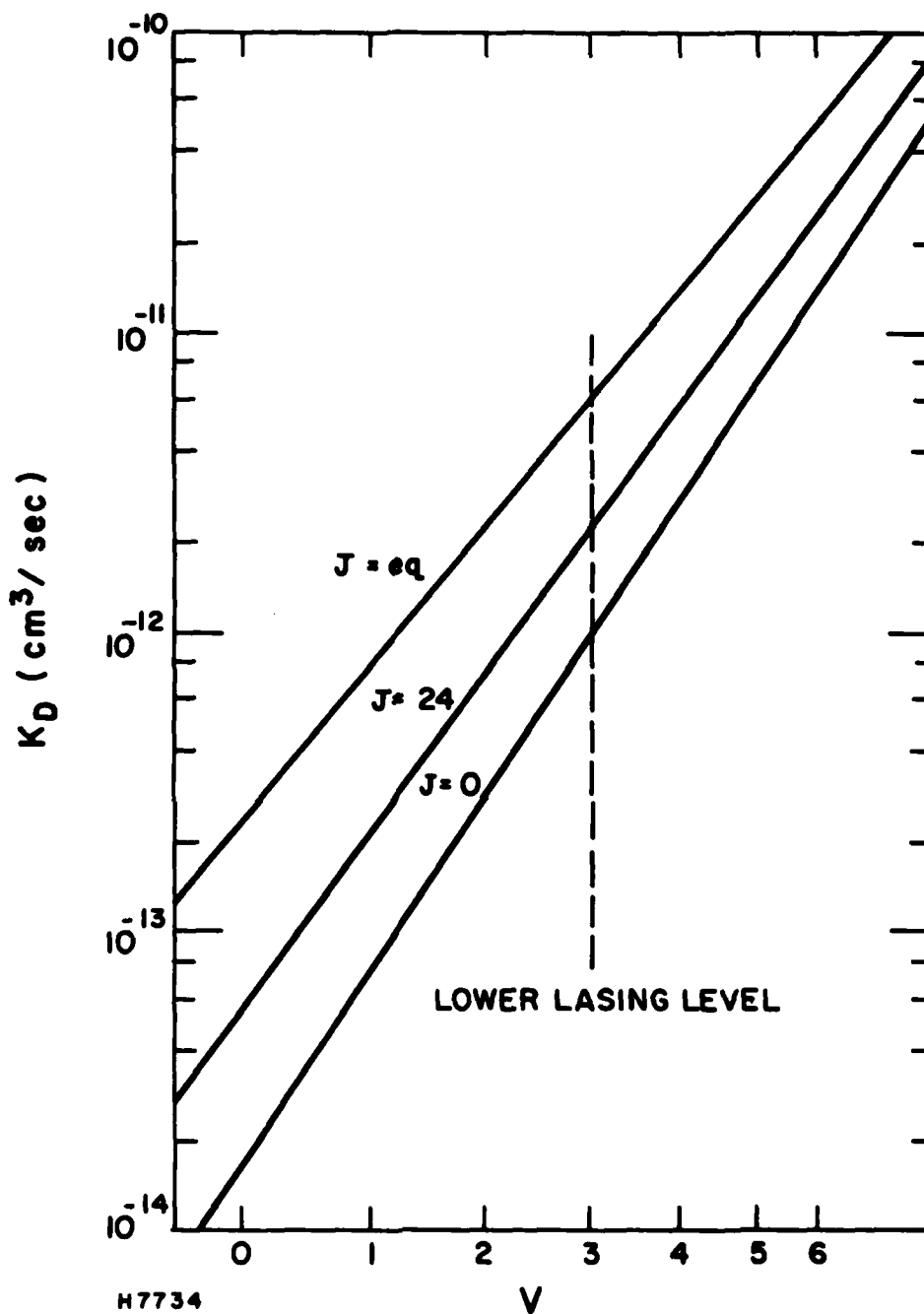


Figure 19. Dissociative Rate Constants for $\text{XeF}(x)$ State at 300°K

In order to test the sensitivity of our results to the translational temperature of the system, one set of runs (with $J=24$) was performed at 450°K . The dissociative rate constants for this temperature, along with the $J=24$ results at 300°K , are shown in Figure 20. The increase in dissociative rate constants is consistent with the observed improvement in XeF laser performance at elevated temperatures.

Again, to alleviate statistical fluctuations, the $V \rightarrow T$, R rate constants were also fitted to an analytical expression of the form

$$k_{v \rightarrow v'} = A \exp(-a\Delta\epsilon)$$

where $\Delta\epsilon = |\epsilon_v - \epsilon_{v'}|$ and $v' > v$. The rate constants for $v' < v$ were obtained by detailed balancing. The fitted constants for our three rotational assumptions at 300°K and the $J = 24$ results at 450°K are given in Table 5. As for the dissociative rate constants, the $V \rightarrow T$, R constants are largest for the equilibrium distribution and smallest for $J = 0$.

The effect that these rate constants are expected to have on the laser performance is discussed in the next section.

D. GROUND STATE BOTTLENECKING

Once the rate constants for ground state deactivation were calculated, they were incorporated into the kinetic equations for the ground state vibrational levels and the two lowest vibrational levels of the B-state in order to determine whether

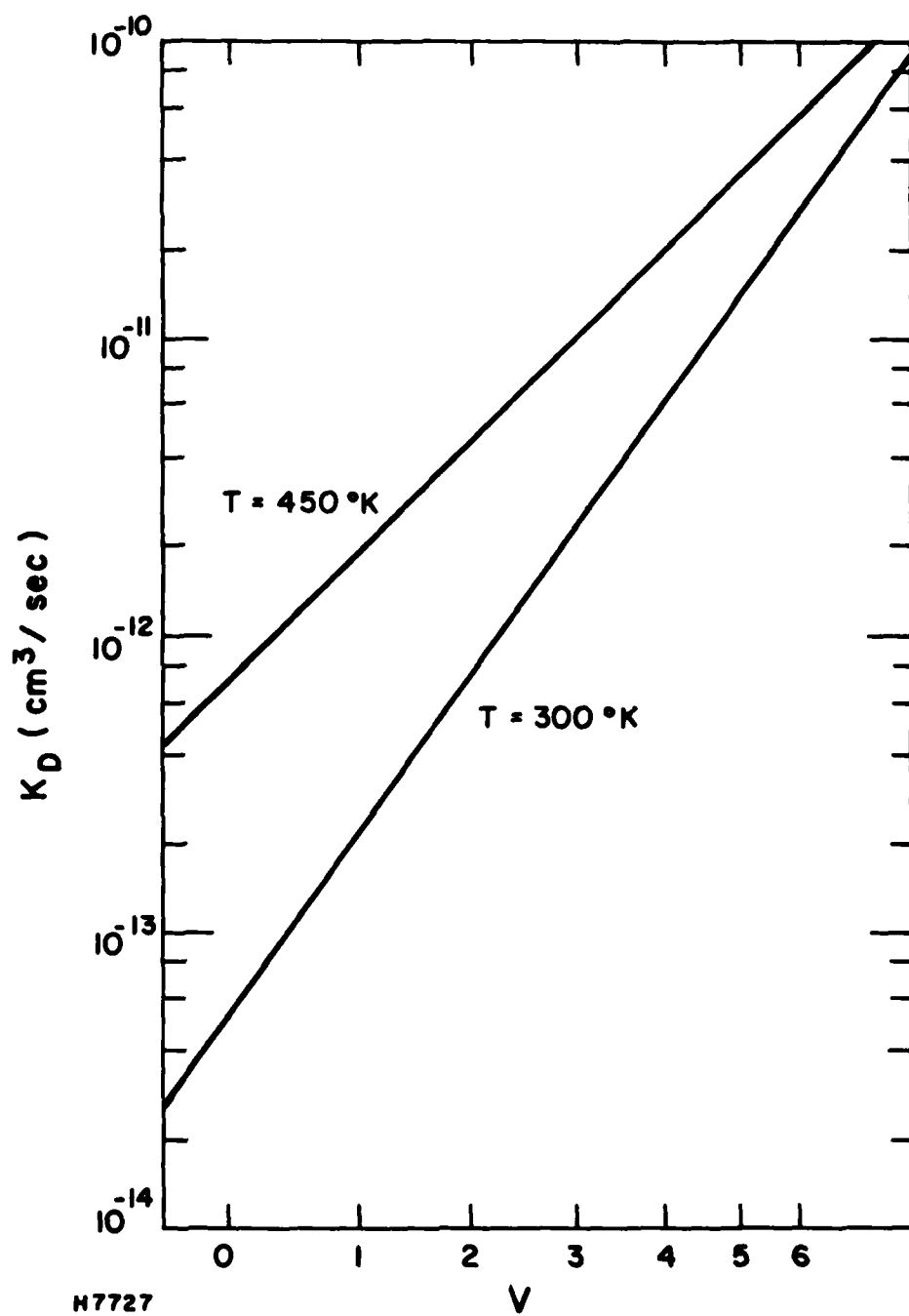


Figure 20. Dissociative Rate Constants for the XeF Ground State at 300°K and 450°K

TABLE 5. V T, R RATE CONSTANTS FOR DIFFERENT
ROTATIONAL DISTRIBUTIONS^{a)}

Case	A (cm ³ /sec)	a (cm)
J = equil., T = 300°K	5.2 x 10 ⁻¹¹	0.0103
J = 0, T = 300°K	2.0 x 10 ⁻¹¹	0.0103
J = 24, T = 300°K	3.7 x 10 ⁻¹¹	0.0109
J = 24, T = 450°K	6.6 x 10 ⁻¹¹	0.0103

a) Rate constants are of the form $k_{vv'} = A_{\text{exp}}(a\Delta\epsilon)$.

these rate constants were sufficiently small to account for the observed low extraction efficiency in the XeF laser. The kinetic equations used are as follows:

For the X state, $v = 0-2, 4-6$

$$\frac{dN_i}{dt} = \frac{F_{0i}N_0^*}{\tau} + \frac{F_{1i}N_1^*}{\tau} + \sum_j k_{ji} N_j N_x - \sum_j k_{ij} N_i N_x - k_{Di} N_i N_x$$

For $v = 3$

$$\begin{aligned} \frac{dN_3}{dt} = & \frac{F_{03}N_0^*}{\tau} + \frac{F_{13}N_1^*}{\tau} + \sum_j k_{j3} N_j N_x - \sum_j k_{3j} N_3 N_x - k_{D3} N_3 N_x \\ & + \frac{\sigma\phi}{h\nu} (N_0^* - N_3) \end{aligned}$$

For the B state

$$\frac{dN_1^*}{dt} = S_1 - \frac{N_1^*}{\tau_D}$$

and

$$\frac{dN_0^*}{dt} = S_0 - \frac{N_0^*}{\tau_D} - \frac{\sigma\phi}{h\nu} (N_0^* - N_3)$$

where N_i and N_i^* are the populations of the i 'th vibrational level of the X and B states respectively, N_x is the neon number density, k_{ji} is the V→T, R rate constant from j to i , k_{Di} is the dissociative rate constant level i , F_{0i} and F_{1i} are the Franck-Condon factors, σ is the stimulated emission cross section, ϕ the cavity flux and S_0 and S_1 are source terms for the B-state

vibrational levels. τ_D is the deactivation lifetime of the B-state and includes both radiative decay and collisional quenching. τ is the feeding term from deactivation of the B-state.

The above equations were solved numerically for different pumping rates, gas mixtures and densities and the results compared to experimental sidelight fluorescence measurements.

These experiments are described in detail elsewhere. (34) Briefly, in this experiment both the output flux and sidelight fluorescence from the B(v'=0)→X(v''=3) transition were measured. The cavity flux was varied by the addition of Cl₂ to an absorption cell located within the optical cavity. This assured that all quenching and formation processes remained constant at all fluxes. A simple steady-state argument leads to the following relation.

$$\frac{N_0^*(o)}{N_0^*} = \frac{1 + \phi/\phi_{sat}}{1 + \frac{1}{\beta} \phi/\phi_{sat}}$$

$N_0^*(o)/N_0^*$ is just the ratio of the sidelight fluorescence without and with lasing. ϕ_{sat} is the saturation flux and β is a parameter that depends on the lower level lifetime. If this lower level lifetime is zero (i.e., no bottlenecking) then $1/\beta \rightarrow 0$ and a plot of $N_0^*(o)/N_0^*$ vs ϕ just a straight line. For a finite lower level lifetime $N_0^*(o)/N_0^*$ will asymptotically approach β for large values of ϕ .

(34) Rokni, M., et. al., Appl. Phy. Lett., to be published

Values of $N_0^*(o)/N_0^*$ obtained from our kinetic equations and experiment are shown in Figure 21. The rate constants for $J=24$ and $J=0$ were used. The hatched areas represent the range of the results when all ground state rate constants are allowed to vary by the factor of two uncertainty in our numbers. It is clear that the $J=24$ values are not sufficiently small to reproduce the experimentally observed fluorescence behavior. While the $J=0$ values marginally reproduce the experimental values, it must be remembered that these constants are expected to be a lower bound on the true values.

From Figure 21, it would appear that the calculated rate constants cannot entirely account for the observed laser behavior. It should be noted that these results depend on measured values of the various B-state quenching rate constants and the stimulated emission cross section and any changes in these values will affect our results. Also, it has been assumed that the $v'=1$ population is unaffected by lasing on the 353 nm transition. Permitting relaxation between these two states would tend to bring our results closer to experiment, but as no fluorescence suppression on the $v'=1$ lines has been observed, this is not a likely answer to the discrepancy. Finally, in our model, it was assumed that rotational relaxation in both the B and X states was instantaneous. Using a more realistic assumption would, again, bring our theoretical model into closer agreement with experiment.

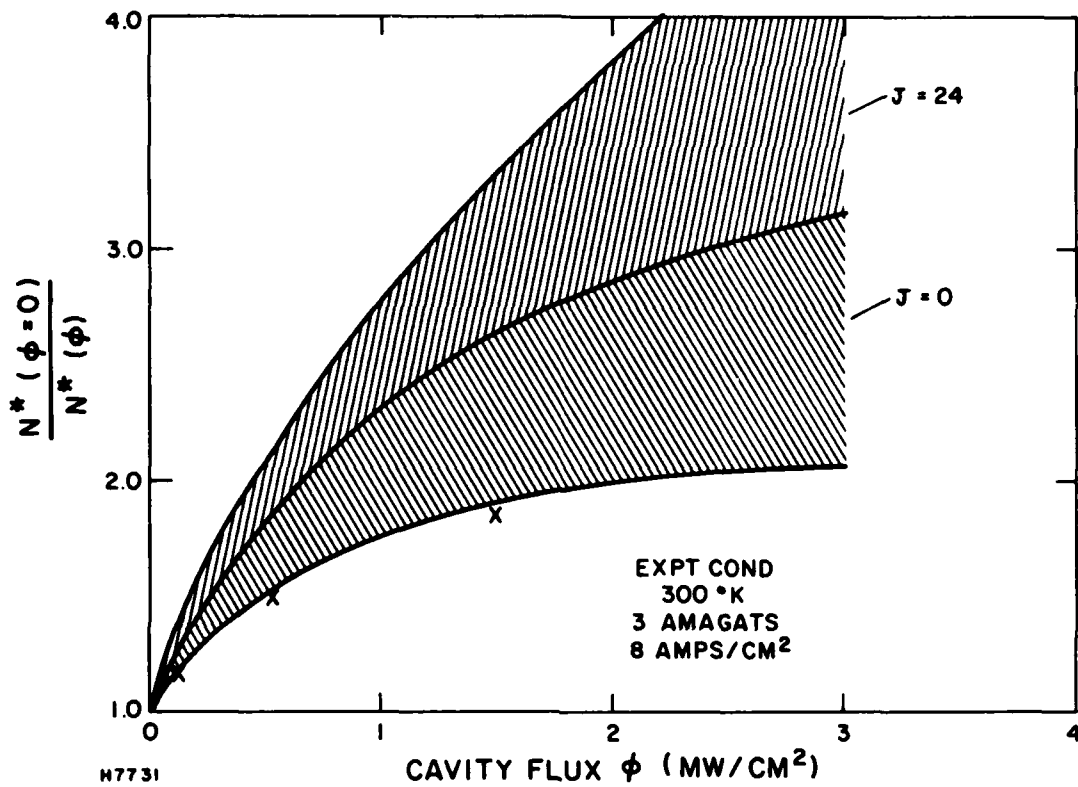


Figure 21. Comparison Between Experimental (x) and Theoretical (Hatched) Sidelight Fluorescence Results for 3 Amagats and an E-Beam Current Density of 8 A/cm²

REFERENCES

1. Parks, J.H., Appl. Phys. Lett. 31, 192 (1977).
2. Tang, K.Y., et al., Appl. Phys. Lett. 32, 226 (1978).
3. Mangano, J.A., Jacob, J.H., Private Communication.
4. Medhekar, A.K., et al., Chem. Phys. Lett. 65, 600 (1979).
5. Shui, V.H., Appl. Phys. Lett. 34, 203 (1979).
6. Jacob, J.H., Private Communication.
7. Mangano, J.A., et al., "One-Meter KeF Laser System" Semi-Annual Report, November 24, 1977 to May 24, 1978.
8. Srivastava, B.N., et al., Appl. Phys. Lett. 32, 705 (1978).
9. Hyman, H.A., Private Communication.
10. Hsia, J.C. et al., "One-Meter KrF Laser System," Semi-Annual Report, Feb. 23, 1977 to Aug. 22, 1977.
11. Rokni, M., Jacob, J.H., Mangano, J.A., Appl. Phys. Lett. 34, 197 (1979).
12. Krause, H.F., et al., Chem. Phys. Lett. 31, 577 (1975).
13. Mandl, A. and Parks, J.H., Appl. Phys. Lett. 33, 498 (1978).
14. Parks, J.H. and Klimek, D., Unpublished.
15. Mandl, A., Private Communication.
16. Mangano, J.A., Unpublished.
17. Mandl, A., Private Communication.
18. Krauss, M., Private Communication.
19. Mangano, J.A., et al., Appl. Phys. Lett. 31, 26 (1977).
20. Jacob, J.H., et al., Appl. Phys. Lett. 33, 109 (1978).
21. Rokni, M., et al., Phys. Rev. 16A, 2216 (1977).

22. Stevens, W.J., Gardner, M. and Karo, A., J. Chem. Phys. 67, 2860 (1977).
23. Wadt, W.R., Cartwright, D.C. and Cowen, J.S., Appl. Phys. Lett., 31, 672 (1977).
24. Mangaon, J.A., et al., "One-Meter KrF Laser System," Semi-Annual Report, 23 Aug. 1976 to 22 Feb. 1977.
25. Keck, J.C., Adv. Chem. Phys. 13, 85 (1967).
26. Bunker, D.L., Methods Comput. Phys. 10, 287 (1971).
27. Shui, V.H., J. Chem. Phys. 58, 4868 (1973).
28. Smith, A.L. and Kobrinsky, P.C., J. Mol. Spect. 69, 1 (1978).
29. Tellinghuisen, P.C., Tellinghuisen, J., Velazco, J.E., Coxon, J.A. and Setser, D.W., J. Chem. Phys. 68, 5187 (1978).
30. Becker, C.H., Casavecchio, P. and Lee, Y.T., J. Chem. Phys. 69, 2377 (1978).
31. Tanaka, Y., and Yoshino, K., J. Chem. Phys. 57, 2964 (1972).
32. Docken, K.K. and Schafer, T.P., J. Mol. Spect. 45, 454 (1973).
33. Abrahamson, A.A., Phys. Rev. 178, 76 (1969).
34. Rokni, M., et. al., Appl. Phy. Lett., to be published.

DISTRIBUTION LIST

Office of Naval Research, Department of the Navy, Arlington, VA 22217 - Attn: Physics Program (1 copy)
 Naval Research Laboratory, Department of the Navy, Washington, D.C. 20375 - Attn: Technical Library (1 copy)
 Office of the Director of Defense, Research and Engineering, Information Office Library Branch, The Pentagon
 Washington, D.C. 20301 - (1 copy)
 U.S. Army Research Office, Box CM, Duke Station, Durham, N.C. 27706 - (1 copy)
 Defense Documentation Center, Cameron Station, Alexandria, VA 22314 - (1 copy)
 Defender Information Analysis Center, Battelle Memorial Institute, 505 King Avenue, Columbus, OH 43201 - (1 copy)
 Commanding Officer, Office of Naval Research Branch Office, 536 South Clark Street, Chicago, IL 60615 - (1 copy)
 New York Area Office, Office of Naval Research, 715 Broadway (5th Floor), New York, NY 10003 -
 Attn: Dr. Irving Rowe (1 copy)
 Air Force Office of Scientific Research, Department of the Air Force, Washington, D.C. 22209 - (1 copy)
 Office of Naval Research Branch Office, 1030 East Green Street, Pasadena, CA 91106 - Attn: Dr. Robert Behringer
 (1 copy)
 Defense Advanced Research Projects Agency, 1400 Wilson Blvd., Arlington, VA 22209 - Attn: Strategic Technology
 Office (1 copy)
 Office Director of Defense, Research and Engineering, The Pentagon, Washington, D.C. 20301 - Attn: Asst. Dir.
 (Space and Adv. Systems) (1 copy)
 Office of the Assistant Secretary of Def., System Analysis (Strategic Programs), Washington, D.C. 20301 -
 Attn: Mr. Gerald R. McNichols
 U.S. Arms Control and Disarmament Agency, Dept. of the State Bldg., Rm. 4931, Washington, D.C. 20451 Attn: Dr. Charles Henkin - (1 copy)
 Energy Research Development Agency, Division of Military Applications, Washington, D.C. 20545 - (1 copy)
 National Aeronautics and Space Admin., Lewis Research Center, Cleveland, Oh 44135 - Attn: Dr. John W. Dunning, Jr.
 Aerospace Research Engineer
 (1 copy)
 National Aeronautics & Space Admin., Code RR, FOB 10B, 600 Independence Ave., SW, Washington, D.C. 20546 - (1 copy)
 National Aeronautics and Space Admin., Ames Research Center, Moffit Field, CA 94035 - Attn: Dr. Kenneth W. Billman
 (1 copy)
 Department of the Army, Office of the Chief of RD&A, Washington, D.C. 20310 - Attn: DARD-DD (1 copy)
 Department of the Army, Office of the Chief of RD&A, Washington, D.C. 20310 - Attn: DAMA-WSM-T (1 copy)
 Department of the Army, Office of the Deputy Chief of Staff for Operations and Plans, Washington, D.C. 20310
 Attn: DAMO-RQD (1 copy)
 U.S. Army Missile Command, Research and Development Division, Redstone Arsenal, AL 35809 - Attn: Army High
 Energy Laser Programs (1 copy)
 Commanding Officer, U.S. Army Mobility Equipment R&D Center, Ft. Belvoir, VA 22060 - Attn: SMEFB-MW (1 copy)
 Commander, U.S. Army Armanent Command, Rock Island, IL 61201 - Attn: AMSAR-RDT (1 copy)
 Director, Ballistic Missile Defense Adv. Technology Center, P.O. Box 1500, Huntsville, AL 35807 -
 Attn: ATC-O (1 copy)
 Director, Ballistic Missile Defense Adv. Technology Center, P.O. Box 1500, Huntsville, AL 35807 -
 Attn: ACT-T
 Commanding General, U.S. Army Munitions Command, Dover, NH 17801 - Attn: Mr. Gilbert F. Chesnov (AMSMU-R) (1 copy)
 Director, U.S. Army Ballistics Res. Lab., Aberdeen Proving Ground, MD 21005 - Attn: Dr. Robert Eichenberger (1 copy)
 Commandant U.S. Army, Air Defense School, Ft. Bliss, TX 79916 - Attn: Air Defense Agency (1 copy)
 Commandant, U.S. Army, Air Defense School, Ft. Bliss, TX 79916 - Attn: ATSA-CTD-MS (1 copy)
 Commanding General, U.S. Army Combat Dev. Command, Ft. Belvoir, VA 22060 - Attn: Director of Material,
 Missile Div. (1 copy)
 Commander, U.S. Army Training and Doctrine Command, Ft. Monroe, VA 23651 - Attn: ATCD-CF (1 copy)
 Commander, U.S. Army Electronics Command, Ft. Monmouth, NJ 07703, Attn: AMSEL-CT-L, Dr. R.G. Buser (1 copy)
 Commander, U.S. Army Combined Arms Combat Dev. Act., Ft. Leavenworth, KS 66027 - (1 copy)
 National Security Agency, Ft., Geo. G. Meade, MD 20755 - Attn: R.C. FOSS A763 (1 copy)
 Deputy Commandant - For Combat and Training Developments, U.S. Army Ordnance Center and School,
 Aberdeen Proving Ground, MD 21005 - Attn: ATSL-CTD-MS-R (1 copy)
 Department of the Navy, Office of the Chief of Naval Operations, The Pentagon 50739, Washington, D.C. 20350 -
 Attn: (OP 982F3)
 Boston Branch Office, Bldg. 114, Section D, 666 Summer Street, Boston, MA 02210 (1 copy)
 Department of the Navy, Deputy Chief of Navy Material (Dev.), Washington, D.C. 20360 -
 Attn: Mr. R. Gaylord (MAT 032B) (1 copy)
 Naval Missile Center, Point Mugu, CA 93042 - Attn: Gary Gibbs (Code 5352) (1 copy)
 Naval Research Laboratory, Washington, D.C. 20375 - Attn: Electro Optical Technology, Program Office,
 Code 1409 (1 copy)
 Naval Research Laboratory, Washington, D.C. 20375 - Attn: Dr. P. Livingston - Code 5560 (1 copy)
 Naval Research Laboratory, Washington, D.C. 20375 - Attn: Dr. A.I. Schindler - Code 6000 (1 copy)
 Naval Research Laboratory, Washington, D.C. 20375 - Attn: Dr. John L. Walsh - Code 5503 (1 copy)
 High Energy Laser Project Office, Department of the Navy, Naval Sea System Command, Washington, D.C. 20360 -
 Attn: Capt. A. Skolnick, USN (PM 22) (1 copy)
 Superintendent, Naval Postgraduate School, Monterey, CA 93940 - Attn: Library (Code 2124) (1 copy)
 Navy Radiation Technology, Air Force Weapons Lab (NLO), Kirtland AFB, NM 87117 (1 copy)
 Naval Surface Weapons Center, White Oak, Silver Spring, MD 20910 - Attn: Dr. Leon H. Schindel
 (Code 310) (1 copy)

DISTRIBUTION LIST (Continued)

Naval Surface Weapons Center, White Oak, Silver Spring, MD 20910 - Attn: Dr. E. Leroy Harris (Code 313) (1 copy)
 Naval Surface Weapons Center, White Oak, Silver Spring, MD 20910 - Attn: Mr. K. Enkenhaus (Code 034) (1 copy)
 Naval Surface Weapons Center, White Oak, Silver Spring, MD 20910 - Attn: Mr. J. Wise (Code 047) (1 copy)
 Naval Surface Weapons Center, White Oak, Silver Spring, MD 20910 - Attn: Technical Library (1 copy)
 U.S. Naval Weapons Center, China Lake, CA 93555 - Attn: Technical Library (1 copy)
 HQ AFSC/XRLW, Andrews AFB, Washington, D.C. 20331 - Attn: Maj. J.M. Walton (1 copy)
 HQ AFSC (DLCAW), Andrews AFB, Washington, D.C. 20331 - Attn: Maj. H. Axelrod (1 copy)
 Air Force Weapons Laboratory, Kirtland AFB, NM 87117 - Attn: LR (1 copy)
 Air Force Weapons Laboratory, Kirtland AFB, NM 87117 - Attn: AL (1 copy)
 HQ Aeronautical Systems Div., Wright Patterson AFB, OH 45433 - Attn: XRF - Mr. Clifford Fawcett (1 copy)
 Rome Air Development Command, Griffiss AFB, Rome, NY 13440 - Attn: Mr. R. Urtz (OCSE) (1 copy)
 HQ Electronics Systems Div. (ESL), L.G. Hanscom Field, Bedford, MA 01730 - Attn: Mr. Alfred E. Anderson (XRT) (1 copy)
 HQ Electronics Systems Div. (ESL), L.G. Hanscom Field, Bedford, MA 01730 - Attn: Technical Library (1 copy)
 Air Force Rocket Propulsion Lab., Edwards AFB, CA 93523 - Attn: B.R. Bornhorst, (LKCG) (1 copy)
 Air Force Aero Propulsion Lab., Wright Patterson AFB, OH 45433 - Attn: Col. Walter MOE (CC) (1 copy)
 Dept. of the Air Force, Foreign Technology Division, Wright Patterson AFB, OH 45433 - Attn: PDTN (1 copy)
 Commandant of the Marine Corps., Scientific Advisor (Code RD-1), Washington, D.C. 20380 (1 copy)
 Aerospace Research Labs., (AP), Wright Patterson AFB, OH 45433 - Attn: Lt. Col. Max Duggins (1 copy)
 Defense Intelligence Agency, Washington, D.C. 20301 - Attn: Mr. Seymour Berler (DTIB) (1 copy)
 Central Intelligence Agency, Washington, D.C. 20505 - Attn: Mr. Julian C. Nall (1 copy)
 Airesearch Manuf. Co., 9851-9951 Sepulveda Blvd., Los Angeles, CA 90009 - Attn: Mr. A. Colin Stancliffe (1 copy)
 Atlantic Research Corp., Shirley Highway at Edsall Road, Alexandria, VA 22314 - Attn: Mr. Robert Naismith (1 copy)
 Battelle Columbus Laboratories, 505 King Avenue, Columbus, OH 43201 - Attn: Mr. Fed Tietzel (STPIAC) (1 copy)
 Bell Aerospace Co., Buffalo, NY 14240 - Attn: Dr. Wayne C. Solomon (1 copy)
 Boeing Company, P.O. Box 3999, Seattle, WA 98124 - Attn: Mr. M.I. Gamble (2-,460,MS 8C-88) (1 copy)
 Electro-Optical Systems, 300 N. Halstead, Pasadena, CA 91107 - Attn: Dr. Andrew Jensen (1 copy)
 General Electric Co., Space Division, P.O. Box 8555, Philadelphia, PA 19101 - Attn: Dr. R.R. Sigismonti (1 copy)
 General Electric Co., 100 Plastics Avenue, Pittsfield, MA 01201 - Attn: Mr. D.G. Harrington (Rm. 1044) (1 copy)
 Hercules, Inc., Industrial Dept., Wilmington, DE 19899 - Attn: Dr. R.S. Voris (1 copy)
 Hercules, Inc., P.O. Box 210, Cumberland, MD 21502 - Attn: Dr. Ralph R. Preckel (1 copy)
 Hughes Research Labs., 3011 Malibu Canyon Road, Malibu, CA 90265 - Attn: Dr. D. Forster (1 copy)
 Hughes Aircraft Co., Aerospace Group-Systems Division, Canoga Park, CA 91304 - Attn: Dr. Jack A. Alcalay (1 copy)
 Hughes Aircraft Co., Centinela and Teale Streets, Building 6, MS E-125, Culver City, CA 90230 -
 Attn: Dr. William Yates (1 copy)
 Institute for Defense Analyses, 400 Army-Navy Drive, Arlington, VA 22202 - Attn: Dr. Alvin Schnitzler (1 copy)
 Lawrence Livermore Laboratory, P.O. Box 808, Livermore, CA 94550 - Attn: Dr. R.E. Kidder (1 copy)
 Lawrence Livermore Laboratory, P.O. Box 808, Livermore, CA 94550 - Attn: Dr. E. Teller (1 copy)
 Lawrence Livermore Laboratory, P.O. Box 808, Livermore, CA 94550 - Attn: Dr. Joe Fleck (1 copy)
 Los Alamos Scientific Laboratory, P.O. Box 1663, Los Alamos, NM 87544 - Attn: Dr. Keith Boyer (1 copy)
 Lockheed Palo Alto Research Lab., 3251 Hanover Street, Palo Alto, CA 94303 - Attn: L.R. Lunsford,
 Orgn. 52-24, Bldg. 201 (1 copy)
 Mathematical Sciences Northwest, Inc., P.O. Box 1887, Bellevue, WA 98009 - Attn: Dr. Abraham Hertzberg (1 copy)
 Massachusetts Institute of Technology, Lincoln Laboratory, P.O. Box 73, Lexington, MA 02173 -
 Attn: Dr. S. Edelberg (1 copy)
 Massachusetts Institute of Technology, Lincoln Laboratory, P.O. Box 73, Lexington, MA 02173 -
 Attn: Dr. L.C. Marquet (1 copy)
 McDonnell Douglas Astronautics Co., 5301 Bolsa Avenue, Huntington Beach, CA 92647 -
 Attn: Mr. P.L. Klevatt, Dept. A3-830-BBFO, M/Sg (1 copy)
 McDonnell Douglas Research Labs., Dept. 220, Box 516, St. Louis, MO 63166 - Attn: Dr. D.P. Ames (1 copy)
 Dr. Anthony N. Pirri, 30 Commerce Way, Woburn, MA 01801 (1 copy)
 Rand Corp., 1700 Main Street, Santa Monica, CA 90406 - Attn: Dr. C.R. Culp/Mr. G.A. Carter (1 copy)
 Raytheon Co., 28 Seyon Street, Waltham, MA 02154 - Attn: Dr. F.A. Horrigan (Res. Div.) (1 copy)
 Raytheon Co., Boston Post Road, Sudbury, MA 01776 - Attn: Dr. C. Sonnenschien (Equip. Div.) (1 copy)
 Raytheon Co., Bedford Labs, Missile Systems Div., Bedford, MA 01730 - Attn: Dr. H.A. Mehlhorn (1 copy)
 Riverside Research Institute, 80 West End Street, New York, NY 10023 - Attn: Dr. L.H. O'Neill (1 copy)
 Riverside Reserach Institute, 80 West End Street, New York, NY 10023 - Attn: Dr. John Bose (1 copy)

DISTRIBUTION LIST (Continued)

Riverside Reserach Institute, 80 West End Street, New York, NY 10023 - Attn: (HPEGL Library) (1 copy)
Rockwell International Corporation, Rocketdyne Division, Albuquerque District Office, 3636 Menaul Blvd.,
Ne, Suite 211, Albuquerque, NM 87110 - Attn: C.K. Kraus, MGR. (1 copy)
Sandia Corp., P.O. Box 5800, Albuquerque, NM 87115 - Attn: Dr. Al Narath (1 copy)
Stanford Reserach Institute, Menlo Park, CA 94025 - Attn: Dr. F.T. Smith (1 copy)
Science Applications, Inc., 1911 N. Ft. Meyer Drive Arlington, VA 22209 - Attn: L. Peckham (1 copy)
Science Applications, Inc., P.O. Box 328, Ann Arbor, MI 48103 - Attn: R.E. Meredith (1 copy)
Science Applications, Inc., 6 Preston Court, Bedford, MA 01703 - Attn: R. Greenberg (1 copy)
Science Applications, Inc., P.C. Box 2351, La Jolla, CA 92037 - Attn: Dr. John Asmus (1 copy)
Systems Science and Software, P.O. Box 1620, La Jolla, CA 92037 - Attn: Alan F. Klein (1 copy)
Systems Consultants, Inc., 1050 31st Street, NW, Washington, D.C. 20007 - Attn: Dr. R.B. Keller (1 copy)
Thiokol Chemical Corp., Wasatch Division, P.O. Box 524, Brigham City, UT 84302 - Attn: Mr. J.E. Hansen (1 copy)
TRW Systems Group, One Space Park, Bldg. R-1, Rm. 1050, Redondo Beach, CA 90278 - Attn: Mr. Norman Campbell (1 copy)
United Technologies Research Center, 400 Main Street, East Hartford, CT 06108 - Attn: Mr. G.H. McLafferty (1 copy)
United Technologies Reserach Center, Pratt and Whitney Aircraft Div., Florida R&D Center, West Palm Beach, FL 33402,
Attn: Dr. R.A. Schmidke (1 copy)
United Technologies Research Center, Pratt and Whitney Aircraft Div., Florida R&D Center, West Palm Beach, FL 33402,
Attn: Mr. Ed Pinsley
Varian Associates, EIMAC Division, 301 Industrial Way, San Carlos, CA 94070 - Attn: Mr. Jack Quinn (1 copy)
Vought Systems Division, LTV Aerospace Corp., P.O. Box 5907, Dallas, TX 75222 - Attn: Mr. F.G. Simpson, MS254142
(1 copy)
Westinghouse Electric Corp., Defense and Space Center, Balt-Wash. International Airport, Box 746,
Baltimore, MD 21203 - Attn: Mr. W.F. List (1 copy)
Westinghouse Research Labs., Beulah Road, Churchill Boro, Pittsburgh, PA 15235 - Attn: Dr. E.P. Riedel (1 copy)
United Technologies Research, East Hartford, CT 06108 - Attn: A.J. DeMaria (1 copy)
Aireborne Instruments Laboratory, Walt Whitorian Road, Melville, NY 11746 - Attn: F. Pace (1 copy)
General Electric R&D Center, Schenectady, NY 12305 - Attn: Dr. Donald White (1 copy)
Cleveland State University, Cleveland, OH 44115 - Attn: Dean Jack Soules (1 copy)
Exxon Research and Engineering Co., P.O. Box 8 Linden, NJ 07036 - Attn: D. Grafstein (1 copy)
University of Maryland, Department of Physics and Astronomy, College Park, MD 20742 - Attn: D. Currie (1 copy)
Sylvania Electric Products Inc., 100 Ferguson Drive, Montian View, CA 94040 - Attn: L.M. Osterink (1 copy)
North American Rockwell Corp., Autonetics Division, 3370 Miraloma Avenue, Anaheim, CA 92803 -
Attn: R. Gudmundsen (1 copy)
Massachusetts Institute of Technology, 77 Massachusetts Avenue, Cambridge, MA 02138 - Attn: Prof. A. Javan (1 copy)
Lockheed Missile & Space Co., Palo Alto Research Laboratories, Palo Alto, CA 94304 - Attn: Dr. R.C. Ohlman (1 copy)
Polytechnic Institute of New York, Rt. 110, Farmingtondale, NY 11735 - Attn: Dr. William T. Walter (1 copy)